
VISUALIZING NEURONAL STRUCTURES IN THE HUMAN BRAIN VIA DIFFUSION TENSOR MRI

WERNER BENGER

Center for Computation & Technology
at Louisiana State University
Baton Rouge, Louisiana, USA
and
Zuse Institute Berlin (ZIB)
Berlin-Dahlem, Germany
and
Max-Planck Institute for Gravitational Physics
Potsdam, Germany

HAUKE BARTSCH

Mercury Computer Systems
San Diego, California, USA

HANS-CHRISTIAN HEGE

Zuse Institute Berlin (ZIB)
Department of Visualization and Data Analysis
Berlin-Dahlem, Germany

HAGEN KITZLER

Department of Neuroradiology
Dresden University of Technology
Dresden, Germany

Received 17 February 2005.

The authors thank Konrad Polthier, ZIB, for many enlightening discussions on various mathematical aspects and Steve Beck, Center for Computation & Technology at Louisiana State University, for pointing out references on the color-pattern interaction supporting this work.

Address correspondence to Dr. Werner Benger, Zuse Institute Berlin, Takustrasse 7, D-14195 Berlin-Dahlem, Germany. E-mail: benger@zib.de

ANNA SHUMILINA

Department of Mathematics
Technical University of Berlin
Berlin, Germany

ANNETT WERNER

Department of Neuroradiology
Dresden University of Technology
Dresden, Germany

Acquisition, analysis, and visualization of diffusion tensor magnetic resonance imaging (DT-MRI) is still an evolving technology. This article reviews the fundamentals of the data acquisition process and the pipeline leading to visual results that are interpretable by physicians in their clinical practice. The limitations of common approaches for visualizing the retrieved data are discussed and a new statistical method is presented to assess the reliability of the acquired tensor field. A novel visualization method is proposed which is discussed in light of neurophysiological considerations of the perception of colored patterns. It is argued that this method is more accurate for medical data while providing a nearly optimal visual stimulus. The method is evaluated on a patient study with a brain tumor.

Keywords brain tumor study, diffusion-tensor imaging, model validation, neuro-radiology, neurosurgery, pattern recognition, statistical analysis, tensor field visualization

INTRODUCTION

Neurological structures can be explored on behalf of tensor fields. With the recent advances in magnetic resonance image acquisition technology, it became possible to measure the diffusion of hydrogen atoms within live human tissues in a clinical environment. It is interesting to note that the first satisfactory theoretical treatment of Brownian motion, the basis of the diffusion theory that led to the current successes, was made by Einstein (1905) exactly a century ago. The same year gave birth to Einstein's more popular theory of special relativity. It ultimately led to the theory of general relativity (Einstein, 1916; Schutz, 2003) that puzzled so many bright brains with its complex mathematics based on the calculus of tensor fields.

Tensor fields are important because they provide richer expressivity than scalar or vector fields. Thus they are also employed in describing anisotropic diffusion processes as they occur in the human brain.

The mathematical concept of a tensor field is sometimes mystified. This is certainly due to a lack of intuition, as in every day life humans are not trained for a direct conscious perception of tensors—in contrast to, for example, scalars such as temperature or vectors such as velocities. Thus, approaches on depicting tensor fields frequently fall back to known concepts such as vector field visualization.

One common approach is “fiber tracking,” aiming to reveal information about connectivity of brain regions. Based on the assumption of the relatively high directionality of diffusion in white matter, the connection of the principal direction of diffusion within each voxel then results in the pathway of neuronal fibers. Detection and study of such connections is important for understanding of the brain’s functionality. Furthermore, the knowledge of the location of important connecting tracts can be crucial in operation planning for prediction and minimization of brain functional losses after an operation. At present the method of diffusion tensor imaging (DTI) is being explored as a research tool to study brain development, brain tumor, traumatic brain injury, multiple sclerosis, Alzheimer’s disease, schizophrenia, and others. In Alzheimer’s disease, for example, significant connectivity disruptions within the associated white matter tracts were found in the early stages of the disease.

Unfortunately, the strategy of following the principal direction of diffusion tensors is inherently unstable (Westin et al., 2002). This approach is particularly problematic in the presence of noise in the data and when the diffusion process is nearly isotropic. High isotropy may be expected in tumor tissues. Thus, conventional methods need to be critically reviewed.

This article explores an interdisciplinary experimental work involving knowledge bases from computer graphics, biology, applied physics, vision research, medicine, and astrophysics. The goal of this effort is to conceive a new approach to visualizing diffusion tensor fields. The motivation for this visualization approach is to investigate whether it could be used to check a possible infiltration of white matter by a brain tumor.

Brain Tumors

Malignant brain tumors are one of the most virulent forms of cancer and can result in profound physical and cognitive impairments. Regions within the United States comprise an incidence of approximately 200,000 newly diagnosed

primary or metastatic brain tumors each year. About 40,000 of them are primary brain tumors originating from the brain tissues. Although metastatic brain tumors have the greatest incidence rate the glioma group, that is, tumors of neuroepithelial brain tissue, account for 49.2% of all Primary Brain and Central Nervous System Tumors (*Year 2001 Annual Statistics Report, 2001*).

There is a lifetime risk of being diagnosed with a primary malignant brain tumor of 0.66% versus 0.54% and a 0.50% versus 0.41% chance of dying from a brain tumor in males and females, respectively. The 5-year relative survival rate following diagnosis of a primary malignant brain tumor is 32.7% for males and 31.6% for females. However, there is a large variation in survival estimates between different types of brain tumors. Survival generally decreases with older age at diagnosis. Children and young adults have better survival for most histologies (Ries et al., 2002). This makes an early and precise diagnosis and effective treatment of utmost importance in terms of the therapeutic outcome. A high variety of different malignant or non-malignant (benign) types of neuroepithelial tumors make effective treatment complicated. At present, the standard treatments for brain tumors include surgery, radiation therapy, and chemotherapy that may be used either individually or in combination. Imaging the pathology provides the foundation for investigations of the biological behavior of tumors and consequently leads to an improved diagnosis and to a more effective treatment.

Overview

This article discusses how to acquire information about the diffusion of water molecules within brain tissues in vivo and how to use this information effectively to gain insight on neurological structures and pathologies.

The second section reviews the physical and biological principles that allow measuring the diffusion tensor field. The mathematical framework of the diffusion process and its limitations due to the currently available data acquisition technology is discussed. A new analysis tool is presented for validating the measurement results and critically reflects the reliability of certain data presentation approaches.

The third section discusses the issues of visual data presentation for effective information analysis. A novel visualization technique for positive definite tensor fields of rank two, such as the diffusion tensor field, is presented and its support by neuro-physiological considerations on the perception of color patterns is discussed.

The final section discusses the application of the described technology on data sets stemming from a clinical environment. There is particular focus on the diffusion properties of a brain tumor by virtue of the visual appearance as generated by the described methods.

DIFFUSION TENSOR DATA ACQUISITION PROCESS

Basics of Magnetic Resonance Image Acquisition

Magnetic-resonance imaging works by initiating measurable electromagnetic radiation from atomic nuclei within the subject of investigation. Atomic nuclei with an odd number of protons and neutrons possess an angular momentum, called spin, and an electrical charge, which causes the nuclei to act as tiny magnetic dipoles with a specific magnetic momentum. The most frequent dipoles in biological tissues are the single protons that are found as the nuclei of hydrogen atoms within water and fat. When no magnetic field is present, these nuclear spins are randomly oriented. An external magnetic field (as applied in an MRI machine) causes the spins of the atomic nuclei to precess around the field's direction at the so-called *Larmor* frequency. For a single proton this frequency is 42.58MHz/T.

The time-dependent magnetic field of precessing protons (i.e., rotating axis changes with time) will interact with the surrounding matter ("spin-lattice" interaction) and transfer energy, leading to an initial decrease of the precession angle. Ultimately the spin becomes aligned to the magnetic field, resulting in a magnetization of the matter. As a statistical ensemble of nuclei is observed, this magnetization increases exponentially with a time scale T_1 . This energy transfer is faster if the environment contains molecules with magnetic fields close to the proton's Larmor frequency, for example, carbon molecules in fat acids, whereas within pure water this energy transfer is less effective, so the T_1 time is shorter in fat than in pure water.

The macroscopic magnetization is the averaged imbalance of nuclei with spins, which are oriented parallel or antiparallel to the magnetic field. These two orientations correspond to different energy states; the transition energy between both states is related to the Larmor frequency. An electromagnetic radio frequency (RF) pulse with exactly this frequency may be used to flip the spin orientation. The amplitude of this RF pulse determines the flip angle. After switching off this RF pulse, the spins will again precess around the magnetic field axis (with a precession angle as determined by the flip angle), and realign with the magnetic field axis after the longitudinal relaxation time

T_1 . Shortly after the RF pulse, the spins of the nuclei will precess synchronously, resulting in a rotating transversal magnetization. This rotating magnetization field induces electromagnetic radiation, which is used for image generation. Due to inhomogeneities in the local magnetic field caused by large molecules in impure fluids (“spin-spin interaction”) the nuclei will quickly run out of phase, such that the transversal magnetization decays exponentially with a time scale called T_2 . This time scale is always shorter than T_1 .

Both time scales depend on the type of matter and therefore cause contrast during imaging. Typical values for white matter tissues in a human brain with a magnetic field of 1.5 T are around 700–1000 ms for the longitudinal relaxation time T_1 and 61–100 ms for the transverse relaxation time T_2 ; for gray matter the longitudinal relaxation time is about twice, 1000–2000 ms, whereas the transversal relaxation is just a little larger (Hornak, 2004).

For image acquisition, an RF pulse is used to flip the spins by 90° relative to the direction of the external magnetic field. At the same time the spins are aligned in phase, which produces a transversal magnetization. That is, during the precession around the (assumed north) direction of the external magnetic field the spins are moving in step around the equator. Due to local tissue properties the spins will lose their phase alignment over time and spread out along the path of precession; some will be getting slower than others.

After some time τ a second pulse is used to flip the spins by 180° , thereby reversing their direction of precession (illustrated by Figure 1). Now the slower spins will be at the front and after some time the faster spins will catch up with them bringing the spins back in phase. So after some time 2τ

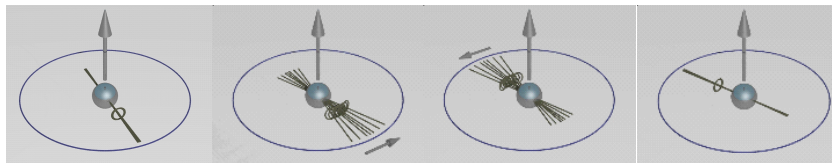


Figure 1. An overlay of several spins during a “spin echo” imaging sequence for MRI. *Left:* after a 90° pulse all spins are aligned, that is, there is a transversal magnetization. *Middle left:* after some time the spins lose their phase alignment because of interactions with the surrounding tissue. *Middle right:* at time $TE/2$, for example, 40 ms (see also the section below on data acquisition), the spins were reversed (apply an 180° pulse). *Right:* at the echo time TE , the phases are aligned again and produce the measurable spin echo. (See Color Plate 29 at end of issue.)

the spins are in phase again and a signal is induced in the receiver coil, which is called the “spin echo.” The procedure of sending a 90° – 180° RF pulse is therefore known as a “spin echo sequence.” As an alternative to the 180° pulse one may also employ a gradient signal to refocus the spins. The resulting “gradient echo” sequence allows shorter data acquisition times.

T_1 , T_2 , T_2^* and Proton Density Weighted Images

The signal at a certain voxel is measured after some echo time TE . Its intensity depends on the relaxation times T_1 , T_2 of the tissues and the proton density PD. Beside the echo time TE and the flip angle (the amplitude of the RF signal), also the time interval (TR, repetition time) between consecutive RF pulses is a steerable data acquisition parameter. Images whose contrast is predominantly caused by differences in T_1 of the tissues are called T_1 -weighted, similar with T_2 and PD. A T_1 -weighted image is achieved by setting $TR \leq T_1$ and $TE \ll T_2$, a T_2 -weighted results from $TR \gg T_1$ and $TE \geq T_2$, and the proton density is measured by $TR \gg T_1$ and $TE \ll T_2$ (cf. Hornak, 2004). T_1 -images provide bright signals for bleedings and fat, whereas T_2 -images show high signal for fluids (see Figure 2 for example). Images retrieved from the much shorter gradient echo sequences measure the signal decay of single echo signals, whereas T_2 is the hull of multiple signals. Such images are called T_2^* -weighted and are used for diffusion measurements.

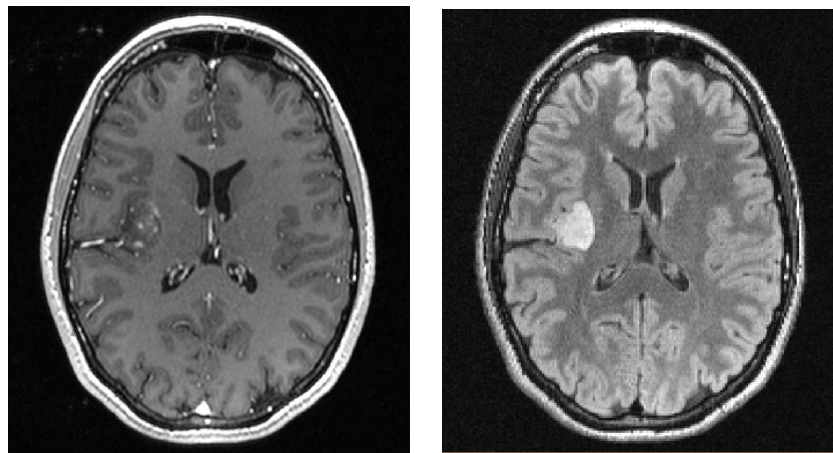


Figure 2. Dataset of a brain harboring a right insular astrocytic tumor, axial slice of T_1 (left) and T_2 (right) MRI measurements.

Measuring Diffusion

Early on it was realized that the MRI technique is also sensitive to motion of the hydrogen nuclei in the tissue. The MR image generation technique is based on measuring the spin echo signal that has been initiated on the nuclei in a certain volume element. However, some of these “marked” nuclei might travel out of the inspected region during the spin echo time. Such motions result in a measurable signal loss for the inspected voxel. This effect occurs in addition to the signal contrast caused by tissue properties visible in T_1 , T_2 , T_2^* and PD. To render MRI sensitive to spin motion effects, the most common approach is to insert equal gradient pulses before and after the 180° -refocusing pulse of a spin echo sequence (see Figure 3). The degree of phase accrual owing to the applied field gradient is proportional to the spin displacement in the direction of the applied gradient. In the absence of motion, the phase shifts due to the two gradient pulses will cancel. If all spins are moving coherently in the field they will acquire identical phase shifts. In case of random displacement, for example, caused by diffusion, the phase shifts accumulated by individual nuclei will differ. The corresponding measurable echo attenuation then depends on the apparent diffusion coefficient as well as on the gradient field’s strength (“b-value”). Using more than one gradient one can probe the full 3-D (stationary) motion at a specific voxel (see Figure 4 for examples).

The gradient measurements still include tissue properties, such as T_1 , T_2 , and so on weighting, depending on the used spin echo sequence (echo and repetition time). To eliminate this dependency, one reference image S_0 (Figure 4, left) is generated without the gradient pulse present but with identical image sequence parameters. Via the mathematical framework described

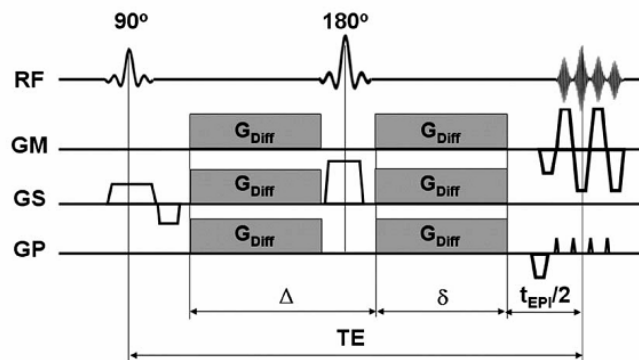


Figure 3. RF sequence sent to retrieve a spin echo gradient signal for a single-shot diffusion-weighted spin echo EPI pulse sequence (for parallel imaging).

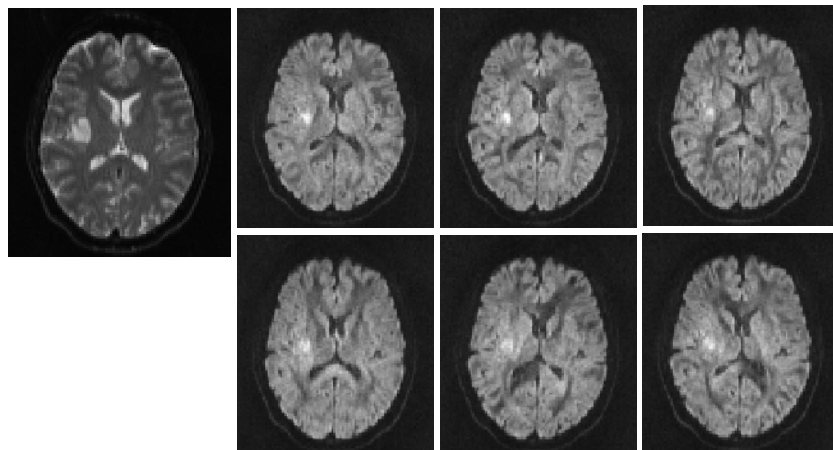


Figure 4. T_2 reference image and measurement with an additional gradient field from six different directions, same dataset as in Figure 2. Regions of high diffusion, such as fluid-filled, appear darker due to signal loss due to moving-out of marked nuclei. The gradient images still involve the effects of the imaging sequence (T_2 shine-through effect). Normalizing by the T_2 image without the diffusion gradient yields a pure diffusion measurement.

in Eq. (7) (later in the article), this reference image is then used to normalize the data, resulting in images that depict motion effects only.

A so-called echo-planar imaging (EPI) pulse sequence samples all the data points after the application of a single RF excitation pulse (or a 90 – 180° RF-pulse combination), therefore allowing acquiring an image within a fraction of a second and minimizing effects of physiologic motion. However, the maximum attainable spatial resolution of EPI can be markedly limited by T_2^* -decay during the long period of data acquisition and is very susceptible to off-resonance effects, such as main field inhomogeneity, local susceptibility gradients, and chemical shift, which all may lead to severe image degradation. A measurement tool to quantitatively assess the reliability of the retrieved data is thus desirable; a possible approach will be described in the next section.

PHYSIOLOGICAL ASPECTS

Separating Diffusion and Perfusion

Intravoxel incoherent motions (IVIM) include molecular diffusion of water as well as the microcirculation of blood in the capillary network (perfusion) (Le Bihan et al., 1988). Whereas molecular diffusion refers to physical properties

of the tissue, microcirculation of blood can be considered as an incoherent motion due to pseudo-random organization of the capillary network at the voxel level. Normally, MR images showing motion effects are quantified by an apparent diffusion coefficient (ADC), which integrates both effects (diffusion and perfusion). However, the echo attenuation due to perfusion is always greater than that due to diffusion, allowing for the separation of both effects on a quantitative basis. If the additional gradient pulses are strong enough, the contribution of the perfusion component to the echo signal can be neglected because the motion effect is large enough that the flowing component becomes invisible. The contribution of diffusion causes just a moderate attenuation of the echo signal, thus allowing acquiring images, which show the diffusion component only.

Diffusion Anisotropy in Brain Tissues

Brain tissues are made up of two basic types of cells: neurons, which are responsible for transmission and processing of neural signals, and glial cells, which significantly outnumber neurons and to which mainly auxiliary functions are ascribed, such as support and nutrition.

A typical neuron consists of a body with a long sprout, called an axon, which transmits signals to remote neurons. The length of an axon can exceed the size of the neuron body by a factor of a hundred-thousand times. In order to increase the transmission speed of electrical impulses, axons are often myelinated. The myelin sheath is built by a special type of glia cells and primarily consists of alternating lipid and protein layers. The regions with prevailing myelinated axons represent the white matter of the brain, whereas neuronal bodies dominate the gray matter.

Thus the white matter represents fiber tracts, connecting remote processing parts of the brain. Diffusion tensor imaging gives a key to explore this brain connectivity and structural reorganizations in malformations due to the brain diseases. Water diffusion across cell membranes is significantly hindered due to their lipid nature. The Myelin sheath additionally prohibits diffusion through axon walls. Therefore, in the regions where bundles of fibers run in parallel, diffusion in the direction of fibers prevails, resulting in diffusion anisotropy. The apparent anisotropy within one voxel will be decreased when averaging over multiple axons running in different directions. Despite this averaging process some structures with pronounced tendency to planar or directional anisotropy are observable.

Tumors mainly consist of glial cells, which are more compact in contrast

to elongated neuronal fibers and thus should be characterized by more isotropic diffusion. Changes in the blood-brain barrier, caused by a tumor, lead to extravasation of intravascular fluid and subsequent accumulation in extracellular space. Thus changed diffusion rates in brain tumor tissues may also be expected. For studying tumor properties and its interaction with surrounding matter, one therefore needs to depict the shape of the diffusion tensor field (its anisotropy properties) as well as its trace, the apparent diffusion coefficient (ADC).

DESCRIBING DIFFUSION VIA TENSOR FIELDS

The MR gradient measurements are fitted to match the properties of a diffusion equation. In thermodynamics anisotropic diffusion of a medium described by a scalar density function $\Phi(x, t)$ (e.g., the time-dependent concentration of water molecules) is modeled by the equation:

$$\frac{\partial \Phi(x, t)}{\partial t} = \nabla \cdot \mathbf{D}[\nabla \Phi(x, t)] \quad (1)$$

where \mathbf{D} is the flux, a function of the concentration gradient $\nabla \Phi(x, t)$. In the simplest case of isotropic diffusion the flux is a multiple of the concentration gradient, that is, $\mathbf{D}[\nabla \Phi(x, t)] = D \nabla \Phi(x, t)$. This diffusion coefficient D is related to the thermal speed of the diffusing particles \bar{v} and their mean free path $l_{mfp} = 1/n\sigma$ (depending on the matter particles per volume n and the cross-section area σ) via

$$D = \frac{3\pi}{16\sqrt{2}} \bar{v} l_{mfp} \quad (2)$$

As the cross-section area might depend on the direction, in general the anisotropic case has to be dealt with. Here, the flux $\mathbf{D}(\mathbf{v})$ can be expanded into a Taylor series (written in a coordinate basis $\{\mathbf{e}_i\}$ using the Einstein sum convention: implicit summation over repeated indices, whereby comma denotes partial derivative by a coordinate function):

$$\mathbf{D}(\mathbf{v}) \equiv \sum D_i(\mathbf{v}) \mathbf{e}_i = \left[D_i(0) + D_{i,j}(0) v_j + \frac{1}{2} D_{i,j,k}(0) v_j v_k + \frac{1}{3} \dots \right] \mathbf{e}_i \quad (3)$$

An overall constant flux $D_i(0)$ vanishes in the diffusion Eq. (1). The second term $D_{i,j}(0)$ constitutes the components of a tensor of rank two. Note that only its symmetric part contributes. In a certain coordinate system it is represented

numerically by a 3×3 matrix, as demonstrated in Figure 5. Due to its symmetry, it contains six independent components. For simplicity the second-rank tensor frequently is just called the “diffusion tensor.” As the particles travel forward only, that is, $\mathbf{v} \cdot \mathbf{D}(\mathbf{v})$ is always positive for all \mathbf{v} , the diffusion tensor is positive definite. Tensors of higher rank may be used to model the diffusion process with higher precision, but a practical limit is given by the number of available gradient measurements. With just six measurements the model is restricted to second order.

Tensors of rank two also occur in other scientific domains such as computational fluid dynamics (CFD) and general relativity (GR) (Einstein, 1916). The stress tensor in CFD is not positive definite, whereas the metric tensor (the central quantity for describing a spacetime) in GR is positive definite. Exploring similarities among the diffusion tensor field in medical imaging and the tensor framework in other sciences leads to interesting inspirations on both sides (e.g., O’Donnell et al., 2002). Later in this article a visualization method is presented that was originally developed for application on astrophysical data sets stemming from general relativity.

The solution of the diffusion equation in one-dimensional space can be described by the convolution of an initial condition $\Phi_0(x)$ and Gaussian kernel $G_{2D_r}(x)$ as

$$\phi(x,t) = \phi_0(x) * G_{2D_r}(x) \quad (4)$$

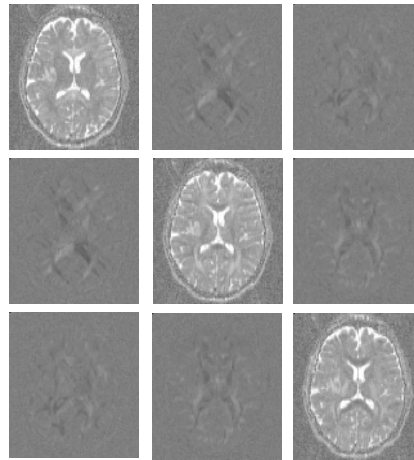


Figure 5. Matrix of tensor images at the axial slice, same dataset as in Figure 2. The 3×3 matrix is symmetric, such that only six of the nine images are independent. Note that due to the negative logarithm in (7) here the gray scale is directly proportional to the diffusion velocity, whereas the MR signal (Figure 4) is reduced by diffusion effects.

with

$$G_{2Dt}(x) = \frac{1}{\sqrt{2\pi Dt}} \exp(-x^2/2Dt) \quad (5)$$

The scalar field $\Phi(x,t)$ can also be interpreted as a probability distribution. The larger the diffusion coefficient, the larger is the diffusion probability in a certain direction. In biological tissues, this will be the case when cells are small or there are few cells per volume due to the increased mean free path. The half width of the Gaussian kernel is $\sigma = \sqrt{Dt}$, that is, an initial concentration peak dissolves in time. When modeling the diffusion equation up to second order, the surface of equal probability is an ellipsoid. Higher orders yield more complex shapes, that is, cubic, quartic and so on surfaces (including superquadrics such as those of Kindlmann (2004) as special case).

Using an expansion of the flux up to second order, following Stejskal and Tanner (1965) the image data S acquired from an MRI scanner can be modeled as

$$S = S_0 \exp(-b\mathbf{g}^T\mathbf{D}\mathbf{g}) \quad (6)$$

where b is the diffusion weighting factor introduced by (Le Bihan et al., 1986), \mathbf{g} are the normalized gradient vectors and \mathbf{D} is the (2nd order) diffusion tensor. Determining the six independent coefficients of \mathbf{D} requires at least six non-collinear measurements. Additional measurements may be used to reduce noise in the data.

To compute the tensor (see Figure 5 for the result) the analytic solution to the implemented was Stejskal-Tanner equation system as described in Westin et al. (2002). The outer products of the six vectors of the diffusion gradients define a tensor basis \mathbf{G} and using its dual $\tilde{\mathbf{G}}$ we can calculate the diffusion tensor for each voxel via the linear sum

$$\mathbf{D} = \sum_{k=1}^6 \frac{1}{b} [\ln(S_0) - \ln(S_k)] \tilde{\mathbf{G}}_k \quad (7)$$

The dual basis is found by stacking the outer products of the gradients as column vectors in a 6×9 matrix and calculate its pseudo inverse $\tilde{\mathbf{G}} = \mathbf{G}^+$.

It is preferable to compute the pseudo-inverse according to its least-squares optimal solution obtained by singular value decomposition. This increases the numerical stability when one of the eigenvalues nearly vanishes. Note that the pseudo-inverse can also be used if more than six gradient

measurements are obtained from the MR scanner. Equation (7) can easily be extended to incorporate these additional measurements as well.

Quality Measurements for the Tensor Fit

In a practical environment, one might be able to acquire more than six diffusion measurements, but not yet enough to fit a diffusion model of third order. However, one may use these additional measurements to validate the second order model by borrowing methods from the statistics of axial data. This section will demonstrate this novel application using one of these methods for the analysis of diffusion weighted tensor imaging. See Mardia and Jupp (2000) for an overview on statistics of circular data.

With only six gradient measurements any combination of six signals uniquely defines a diffusion tensor. This rank-2 tensor will be sensitive to noise in the measurements. Additional measurements can be used to reduce this sensitivity, but these can also be employed to perform statistical tests in order to validate the local fit to a tensor of rank two. This approach is in contrast to a spatial smoothing which is used in order to improve, for example, by smoothing the diffusion tensor field.

A first test that can be performed on the data is a test in order to reject the hypothesis of isotropy. Whenever the hypothesis of isotropy may be rejected in the data, the tensor has a dominant direction. In contrast, a voxel for which we cannot reject the hypothesis the diffusion may be isotropic and derived quantities such as the maximum eigenvector are highly sensitive to noise in the measurements. The hypothesis can be rejected given a specific probability and thus is a quantitative assessment of the quality of the eigenvector decomposition, that is, the eigenvector direction is not reliable in regions of low probability. This information is of crucial relevance for the reliability of visualization techniques that are based on such derived quantities, for example, the computation of integral lines of the maximum eigenvector, as frequently employed for fiber tracking.

A simple test for isotropy of an axial distribution is the Bingham test (Bingham, 1974). A distribution function can be obtained from the diffusion tensor \mathbf{D} by rescaling its eigenvalues to $\text{tr}(\mathcal{D}) = 1$. Now the $p \times p$ matrix \mathcal{D} is compared with its expected value $p^{-1}\mathbf{I}$ where \mathbf{I} is the identity matrix. Given that n is the number of measurements taken isotropy is rejected for large values of

$$S = \frac{p(p+2)}{2} n \left(\text{tr}(\tilde{\mathbf{D}}^2) - \frac{1}{p} \right) \quad (8)$$

According to Jupp (2001) this test can be improved by using the modified Bingham test statistic:

$$S^* = S \left(1 - \frac{1}{n} (B_0 + B_1 S + B_2 S^2) \right) \quad (9)$$

where

$$B_0 = \frac{p^2 + 6p + 20}{12(p + 4)} \quad B_1 = \frac{-(p^2 + 3p + 8)}{3(p + 4)(p^2 + p + 2)} \quad (10)$$

$$B_2 = \frac{p^2 - 4}{3(p + 4)(p^2 + p + 2)(p^2 + p + 6)}$$

In this case

$$S^* = \chi_{(p-1)(p+2)/2}^2 \quad (11)$$

with an error of order $O(n^{-3/2})$. See Table 1 for a list of values used in this study.

Tuch and colleagues (1999) used the (Pearson) correlation coefficient between the measured diffusion coefficient and the diffusion coefficient as reconstructed from the 2nd order diffusion tensor (the evaluation of the diffusion tensor in the direction of the measured gradient). The measure is normalized by the mean and variance of the two variables and large values indicate a good (linear) match of the 2nd order model to the data.

Interpolation of Tensor Fields

In DT-MR imaging the physical tensor diffusion field in continuous space is sampled at the centers of the voxel grid, that is, at discrete locations. In practice an ideal sampling is not achieved, but due to the finite resolution of sensors, information is collected from a certain volume around each point. The signal formation process can in general be described by a convolution of the true physical signal with the point-spread function of the recording device. This results in a blurring of the signal where fine details are lost. Additionally noise is superposed, originating from the thermal Brownian motion of electrons in the various electronic components of the measuring device. The raw

Table 1. χ_5^2 statistics for a number of probabilities α

α	0.5	0.10	0.05	0.02	0.01	0.001
χ_5^2	4.351	9.236	11.07	13.388	15.086	20.517

magnetization signals are transformed by Fourier transformation and solving the Stejskal-Tanner equations to the diffusion tensor. Thus noise propagation is difficult to model and it is even more tedious to reconstruct the continuous diffusion tensor field from the finite set of sample values. The measured tensor in each voxel thus is inherently a noisy, discrete, and volume-averaged quantity.

For visualization, one remedy is to depict only the tensors at the discrete sample locations, using individual graphical elements (splats, icons). However, other visualization techniques, in particular the fiber tracking method, which is based on computation of the integral lines of the eigenvector field, require tensor values at arbitrary locations in space. Therefore the crucial question arises, how to reconstruct the continuous tensor diffusion field from the sampled points. Intuitively it is clear that structures approximately the scale of the sampling distance or finer are lost and no additional information can be gained by reconstructing a continuous field. In image processing reconstruction is done by interpolation—using linear interpolation, or cubic or quintic spline interpolation, radial basis functions and sinc-based interpolation techniques (see, e.g., Jähne, 1997; Lehmann et al., 1999; Unser et al., 1992; Unser et al., 1993a; Unser et al., 1993b; Lehmann et al., 2001; Meijering, 2002)—or if noise effects are considered too, by approximation, for example, using some variational regularization methods that minimize an energy containing a similarity term and a smoothness term (Rudin et al., 1992; Osher et al., 2003; Lysaker et al., 2003). All these methods work for scalar images. In tensor image processing often such methods are applied to individual tensor components. This of course is a questionable method.

Not much research has been done so far for interpolation methods of tensor fields. Aldroubi and Basser (1999) present a mathematical basis for a continuous approximation of symmetric tensor fields with noise reduction using Wiener amalgam spaces. In Pajevic et al. (2002) it is shown that this method boils down to repeated application of 1-D B-spline transforms and it is applied to DT-MRI data. It introduces uniform and isotropic smoothing in the data and is incapable of dealing with discontinuities. The smaller structures will be distorted at the levels of smoothing required to alleviate the noise effects. To achieve a more efficient approximation in Pajevic et al. (2005) the tensor field approximation method is extended to non-uniform rational B-splines (NURBS). Only recently it has been shown how to devise an interpolation method that conserves positive definiteness by interpolating in the Riemannian symmetric space of positive definite tensors (Moakher & Batchelor, 2005). Finally, in Weickert (2005) a PDE-based unified model for image

interpolation and approximation is extended to tensor data. The novel technique is based on anisotropic diffusion. It allows discontinuity-preserving interpolation with no additional oscillations and it respects positive semidefiniteness.

DT-MRI fiber tractography is based on integration of field lines tangential to the local eigenvector associated with the maximal eigenvalue. Integrating a noisy direction vector field can cause these computed fiber trajectories to wander off course. Additionally, in regions with nearly isotropic tensors, noise effects significantly determine the classification of eigenvectors as an eigenvector with a maximal eigenvalue. Thus in less coherently organized matter regions and at low signal-noise-ratio this creates significant numerical instabilities. Specific methods have been devised, for example, to handle the indeterminacy of the sign of the eigenvector (causing erratic forward and backward steps as the path integration proceeds) and to detect misclassified eigenvectors due to missorted eigenvalues in regions with only little anisotropy (causing the trajectory suddenly to veer off course), (see, e.g., Weinstein et al., 1999; Basser et al., 2000). Nevertheless, it comes as no surprise that the results strongly depend on the interpolation technique and the numerical integration method used.

For illustration, some examples on the effects of using different interpolation schemes are shown in Figure 30 later in the article. They are based on the tensor field visualization method presented later. These interpolation methods use component-wise interpolation. Specifically designed tensor field interpolation methods, which, for example, conserve anisotropy, might somewhat improve the fidelity of tract-following schemes. However, a “perfect” interpolation scheme is hard to suggest, because there is no guarantee that, for example, conservation of a property, like, for example, anisotropy, reflects the underlying diffusion field more truly. The fundamental flaw in the concept of a principal eigenvector field cannot be dispelled: in regions with isotropic tensors (for data without noise) or with regions of almost isotropic tensors (for data with noise), the principal eigenvector field of the underlying diffusion field is not well defined.

Due to this fact, the widely followed approach of fiber tracking was considered to be unreliable. Especially for usage in medical applications the method seems to be questionable. A method that computes fiber trajectories should only display reliable information and at least depict uncertainties in the process. Instead, the authors propose a visualization approach that displays the data in a way that is inherently robust. This method will be discussed in the next section.

VISUALIZING TENSOR FIELDS

An intuitive way to depict a diffusion tensor is to consider its associated propagation surface. For tensors of rank two, the surface of equal propagation is an ellipsoid. DT-MRI measurements directly provide propagation distances, such that the square roots of the tensor's eigenvalues yield the propagation ellipsoid's half axes. The ellipsoid visualizes the diffusion coefficients in each direction, as demonstrated in Figure 6. Equally appropriate is the visualization of its inverse, which enhances various regions of the tensor field more clearly (Figure 6, right), although the physical interpretation should then be reversed (indication of MR spin echo signal instead of diffusivity).

The structure of the diffusion tensor is contained in this image, but is hard to interpret. For studying the propagation properties, the lengths of the three half-axis and three rotation angles of each ellipsoids may be computed via eigenvalue decomposition. These six numbers form an alternative, unique set for describing the ellipsoids. The three eigenvalues are shown in Figure 7. The brightness of each pixel depicts the strength of water diffusion, where the maximum eigenvalue (left) indicates its maximal speed, the minimal eigenvalue (right) its minimal speed, and the median eigenvalue (center) the speed in the remaining direction. It is important to note that in some regions the minimal speed is similar to the maximal speed. In these isotropic regions, water diffusion may occur in all directions equivalently and the maximum eigenvector becomes undefined. Taking into account noise during data acquisition, the maximal eigenvector has to be considered unreliable also in just slightly

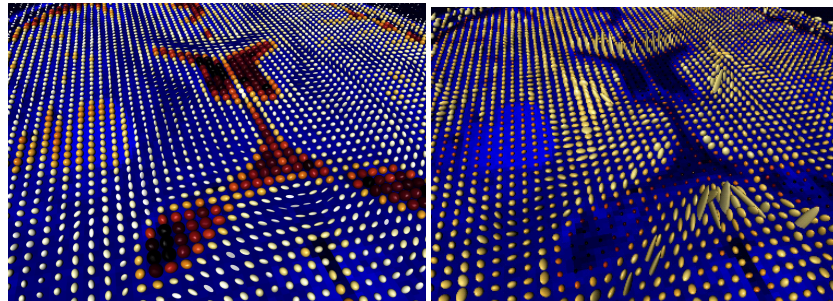


Figure 6. Propagation surfaces (*left*) and MR signal (*right*) of the diffusion tensor in a three-dimensional view of the axial plane on top of a T_2 image (in blue), same dataset as in Figure 2. Diffusion is large where the spin echo is small and vice versa. Both effects are described by tensors, which are inverse to each other. Color indicates trace (absolute velocity). The tumor's fast, isotropic diffusion is visible on the left. (See Color Plate 30 at end of issue.)

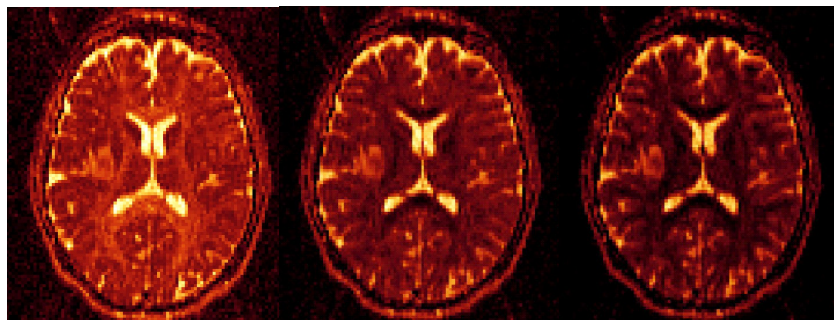


Figure 7. Tensor eigenvalues of same dataset as in Figure 2, depicting an axial slice of the maximal, median and minimal eigenvalue. Note the ringlike appearance of peripheral higher tensor eigenvalues compared to the tumor center in all three expositions. (See Color Plate 31 at end of issue.)

anisotropic regions. A statistical measure as presented in the former section may be used to support or reject the reliability of the maximum eigenvector.

Although the complete information of the diffusion MRI is displayed by tensor ellipsoids, this rendering method does not allow easy visual interpretation. One thus seeks visualization methods that are superior in displaying: (1) global information, such as detecting regions of similar diffusion properties, and (2) deviations from the isotropic case and its variations. For a scalar field, visualization of isosurfaces provides a way to find areas of equal properties. However, there is no equivalent for multivalued tensor fields.

Shape Factors

An intuitively useful classification scheme based on the shape of tensor ellipsoids was invented by Westin (Westin et al., 1997). If one is primarily interested in the directions that are preferred in some tensor field, then the trace (the

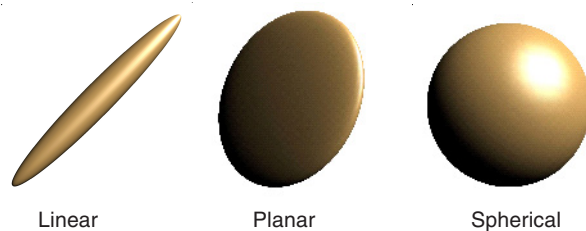


Figure 8. Classification of a tensor ellipsoid by its shape. (See Color Plate 32 at end of issue.)

diagonal of the inverse ellipsoid's bounding box) may be disregarded and just look at the relationship of the tensor's eigenvalues. One may distinguish among the following dominant cases (see Figure 8), based on the tensor's eigenvalues:

1. Linear case: $\lambda_{\max} \gg \lambda_{\text{med}} \approx \lambda_{\min}$, the propagation ellipsoid is similar to a needle along the eigenvector with the dominant eigenvalue. The diffusion coefficients are small in one direction, and equally large in the two perpendicular directions.
2. Planar case: $\lambda_{\max} \approx \lambda_{\text{med}} \gg \lambda_{\min}$, the propagation ellipsoids resembles a flat disc that is spanned by the two eigenvectors with the dominant eigenvalues. Accordingly, the diffusion coefficient is large in one direction and small in the other directions.
3. Spherical case: $\lambda_{\max} \approx \lambda_{\text{med}} \approx \lambda_{\min}$, all eigenvalues are of approximately the same size. No direction is preferred (isotropic case), and the propagation surface is similar to a sphere. The diffusion coefficients are about the same in all directions as well.

An arbitrary tensor \mathbf{D} can be written as a linear combination of these extreme cases. Normalizing the coefficients by the trace $\text{tr}(\mathbf{D}) = \lambda_{\max} + \lambda_{\text{med}} + \lambda_{\min}$ yields numbers that only depend on the ellipsoid's shape independent from its size:

$$c_l = \frac{\lambda_{\max} + \lambda_{\text{med}}}{\lambda_{\max} + \lambda_{\text{med}} + \lambda_{\min}} \quad (12)$$

$$c_p = \frac{2(\lambda_{\text{med}} - \lambda_{\min})}{\lambda_{\max} + \lambda_{\text{med}} + \lambda_{\min}} \quad (13)$$

$$c_s = \frac{3\lambda_{\min}}{\lambda_{\max} + \lambda_{\text{med}} + \lambda_{\min}} \quad (14)$$

The scaling factors 2 and 3 are used such that each shape factor is in the interval (0, 1). Other normalization choices are possible as well. The three shape factors obey the relationship $c_l + c_p + c_s = 1$ and can thus be interpreted as barycentric coordinates within a triangle, as illustrated in Figure 9. The spherical factor c_s is a direct measurement of the anisotropy.

The shape factors of the tensor field may be computed at each point and displayed as a gray-scale image as demonstrated in Figure 10. Regions of high linearity stand out prominently in the c_l image and indicate water diffu-

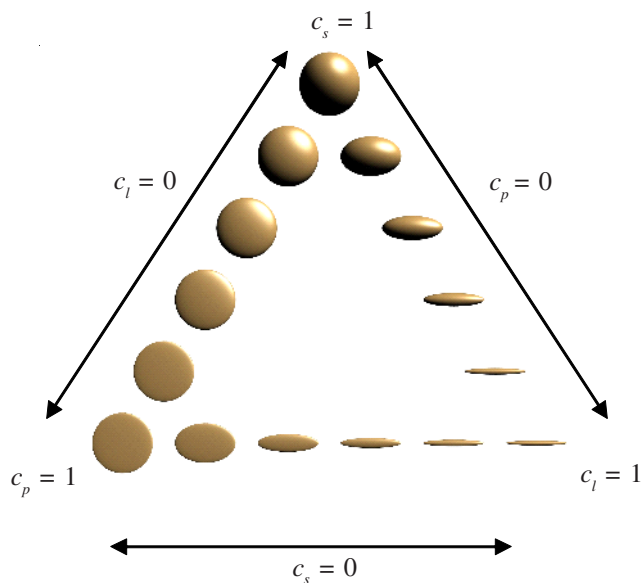


Figure 9. Barycentric shape parameters and their corresponding tensor ellipsoids. The left edge corresponds to zero linearity, bottom edge to zero sphericity, and right edge to zero planarity. (See Color Plate 33 at end of issue.)

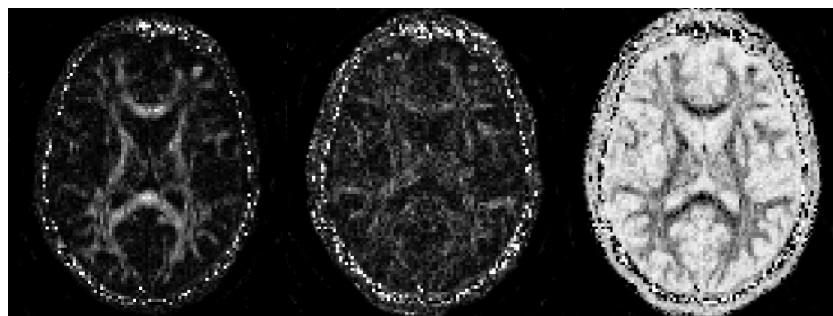


Figure 10. Shape factors of the DTI dataset from Figure 2: Axial slice for linear, planar, and spherical shape factors. Note that the sum of all shape factors always equals unity by construction. The area outside of the brain has been set to black manually for illustration purposes.

sion primarily in one direction. If linear propagation is interpreted to be primarily caused by axonal cells, then the linear shape factor image displays regions of white matter tissue as compared with gray matter tissues. A planar shape factor may indicate crossings of linear propagation regions, which are below image resolution. A spherical shape factor may indicate gray matter as well as crossings of three linear propagation directions. However, in renderings of such scalar one-dimensional quantities the actual direction of diffusion is not visible, which could be relevant to interpretation. Just as little can the absolute diffusion velocity (i.e., the tensor's trace) read off. By theoretical considerations (see the previous section on diffusion anisotropy in brain tissue) one expects to specifically see variations of the apparent diffusion coefficient (the tensor trace) in tumor tissues. Thus, there is a need for better visualization methods that are capable of displaying all tensorial quantities in place at once and that are also sensitive to small variations of each component.

Color Coding

When conceiving a better visualization method, one faces the problem of mapping all six tensorial quantities at each voxel to visualization parameters, even when limiting oneself to a plane instead of an entire volume as first step. Computer graphics models color as triples of red, green, and blue intensities. For displaying all six independent tensorial quantities additional parameters are required. One option is to employ transparency, that is, the attenuation of some background color at each color channel (see Figure 11, left). This approach requires that the viewer is aware of the real background color to mentally separate the transparency from the foreground color of a light emitting voxel. Usual computer graphics such as OpenGL models transparency by a single channel, called the alpha channel, such that the effective parameter space for colorizing a voxel is just four-dimensional.

A possible approach is to map the three components of the major eigenvector to (rgb) colors, and to scale them with the fractional anisotropy, such that regions of high anisotropy stand out brightly and colorful (see Figure 11, right). Recently, Field et al. (2004) used a similar technique to study the influence of brain tumors on the surrounding matter. Kindlmann et al. (2000) investigated strategies for mapping the six tensorial quantities to the four-dimensional color space in an entire volume (see Figure 12). This approach is exact in the sense that it does not add artificial information to the data, but it is also incomplete as it can only display four out of six quantities. Moreover it is not straightforward to interpret, because the mapping of directional

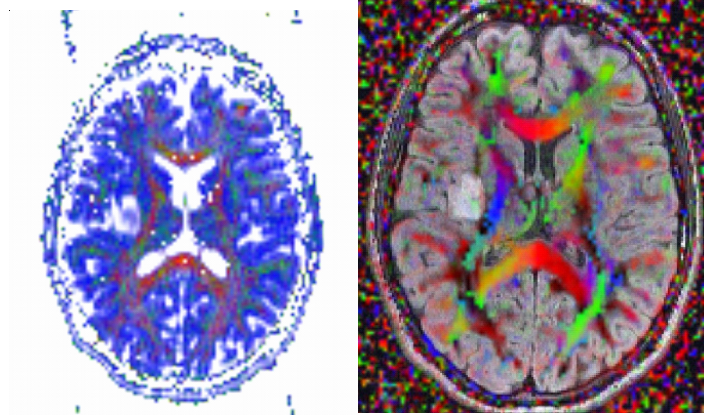


Figure 11. Demonstration of alternative color encodings of the DTI dataset from Figure 2. The left version maps shape factors to red, green, and blue color channels, whereby the tensor's trace is mapped to transparency. This approach displays isotropy information in color, but no directional information is available. The right version employs a directional color map of the major eigenvector, whereby the linear shape factor is used as transparency. A conventional T2 image is used as background for orientation. The close relation of the tumor to the posterior limb of the internal capsule is highlighted then by the blue color of this fiber structure. However, no information about the tensor's trace, that is, absolute diffusion velocity, is available here. (See Color Plate 34 at end of issue.)

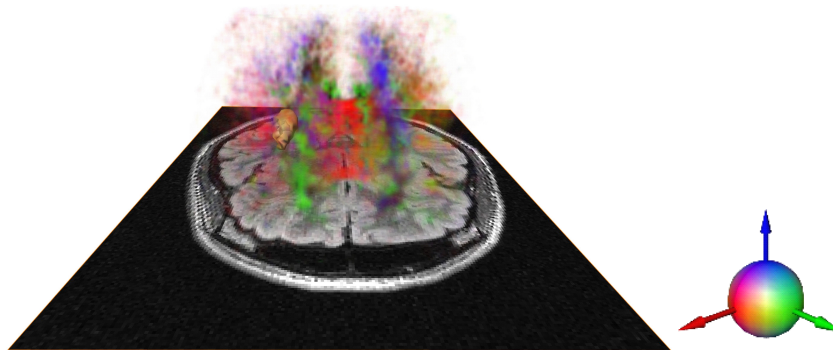


Figure 12. Directional color map used for volume rendering anisotropy, but visually appears like a surface structure even when applied to an entire volume since the perception of reflection within a volume is bad. (See Color Plate 35 at end of issue.)

information to colors requires some mental interpretation and learning effort. Kindlmann and Weinstein (1999) encoded the directional information as reflection properties on a surface: a tensor may be isotropic or anisotropic, and so is diffuse reflection, for example, by a surface of polished metal. This approach provides quite a natural, intuitive way of visualizing anisotropy, but visually appears like a surface structure even when applied to an entire volume since our perception of reflection within a volume is bad.

Visualization via Color Patterns

For visualizing a tensor field in an easily perceptible way, a spatial graphical representation of the tensor's spatial properties is preferable. To display the measured data independent of possible interpolation or integration artifacts (see Figure 30 for illustration), a per-vertex rendering method is advantageous. A graphical primitive that is able to depict a full tensor's information content at a certain point in space is called an "icon." The selection of appropriate visual stimuli is crucial for effective visual communication. Several iconic techniques have been proposed beyond the straightforward quadric surfaces (ellipsoids), such as Haber glyphs (Haber, 1990) or superquadrics (Kindlmann, 2004). All these approaches have in common that the (usually three-dimensional) icons transport color and shape information, resulting into a two-dimensional color pattern on the output medium (screen, hardcopy). One may ask how much information may be packed into a general colored pattern element such that it is still distinguishable from its neighbors. An approach of this kind was used by Laidlaw et al. (1998): Inspired by the oil paintings of Van Gogh, they rendered each data point as a "paint stroke," where each stroke was parameterized by the tensorial quantities.

Psycho-physiological studies indicating color and pattern information are processed in separable neuronal pathways (Poirson & Wandell, 1996). This result may be used to communicate independent data, such as the components of a tensor field, within the same graphical primitive. The dimensionality of the perceptual space of color patterns was studied by Mojsilovic et al. (2000). They discovered five dimensions (ordered by priority):

1. overall color
2. directionality and orientation
3. regularity and placement rules
4. color purity
5. pattern complexity and heaviness

and five similarity rules, which together form a vocabulary and grammar for color patterns. Vision research frequently employs Gabor patches (Gabor, 1946; Watson & Turano, 1995a; 1995b). The present authors found them to be very suitable for tensor field visualization as well. Gabor patches are Gaussian-windowed sinusoidal luminance patterns (see Figure 13), which can be described on a two-dimensional plane (omitting time dependency here) as

$$L(x, y) = L_c (1 + C_p \cos(2\pi xf) e^{-l(x,y)})$$

where L_c is the mean luminosity, C_p the peak contrast, f the spatial frequency and $l(x, y)$ is a distance function within the plane. It may involve a linear transformation (expressible as a matrix) for rotation and scaling:

$$l(x, y) = l_{xx} x^2 + l_{xy} xy + l_{yy} y^2$$

Note that only the symmetric part of the matrix (l) contributes. The eigenvalues of this transformation matrix are then inversely proportional to the Gaussian standard deviation of the luminance distribution. Gabor patches have been used for various experimental investigations in psychophysical studies, especially in motion recognition. Physiological findings support the importance of edgelike stimuli for the human visual system.

It was found that a majority of neurons in early visual cortex (area V1 simple cells) are particularly selective to an oriented edgelike pattern that can be sufficiently described by the Gabor-patch framework (Hubel & Wiesel, 1962; Jones & Palmer, 1987). Analyzing natural images also showed the importance of edges for object recognition. It was shown that edge features define an efficient framework for representing the information content of images (Bell & Sejnowski, 1996).

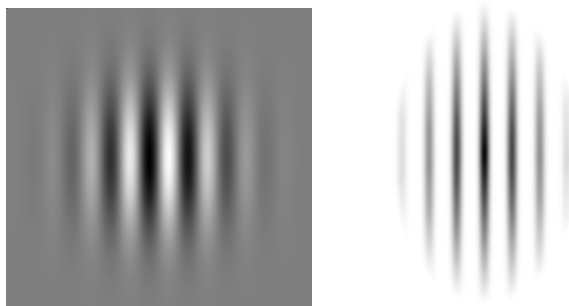


Figure 13. A Gabor patch in its original form (*left*) is a variation of neutral gray. In its transparent version (*right*), only the positive wave is seen because there is no negative transparency. As a tensor pattern primitive, it may also occur in an elliptical variant.

Gabor Patches as Tensor Icons

The authors' approach on tensor field visualization is to map tensorial quantities to texture patterns at each voxel, whereby each of these voxel-sized texture elements resembles a Gabor patch. As these inherently contain directional information, researchers have a natural way of displaying the eigenvector information of the tensor field and incorporating the second dimension of the color pattern's perceptual space, *directionality and orientation*, into the visualization. Static Gabor patches are two-dimensional objects, such that it is natural to draw them on a plane spanned by the two most dominant eigenvectors of the diffusion tensor at each data point. The x-direction of the Gabor patch is aligned with the major eigenvector. The tensor field's major and median eigenvalues λ_{\max} , λ_{med} , hereby directly match the Gabor patch's linear transformation properties $l_{xx} \equiv \lambda_{\max}$ and $l_{yy} \equiv \lambda_{\text{med}}$, whereas $l_{xy} = 0$ because the eigenvectors of the diffusion tensor are orthogonal. The authors set the spatial frequency $f = A/c_l$ to be inversely proportional to the linear shape factor c_l , such that for planar regions $c_l = 0$ the frequency becomes infinite and no directional information is visible on the texture element (Figure 14). For $c_l = 1$, the texture element shall embody a certain spatial frequency,

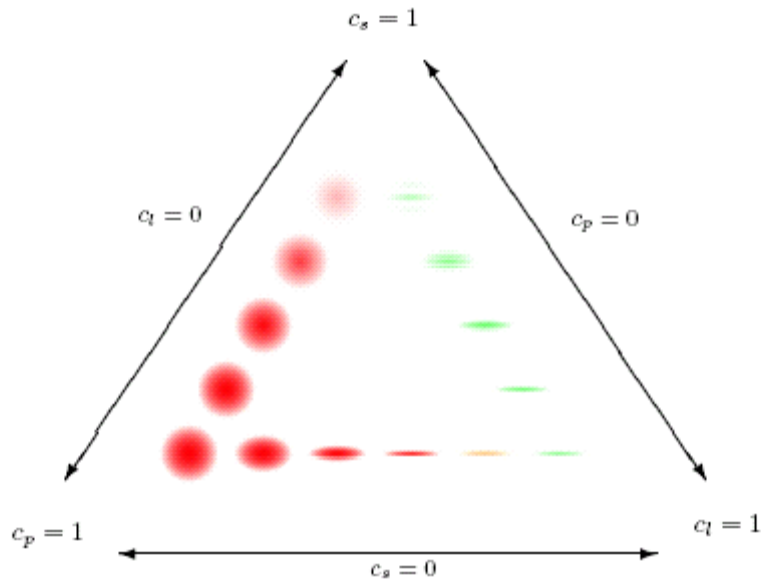


Figure 14. Tensor splats: Colored Gabor patches are used as graphics primitives (“rendering quantum”) to visualize the shape factors of a tensor. (See Color Plate 36 at end of issue.)

which is left as a user-adjustable parameter. The authors freely call A the “Airity” after the astronomer George Airy, who discovered the similarly looking diffraction pattern of a star’s image at the focus of a telescope. Interactive adjustment of the airity allows the user to emphasize areas in the tensor field with low linearity.

When basing a visualization method on the dominance of eigenvectors, one needs to carefully consider regions where there is no such dominance, that is, eigenvectors become ambiguous. This happens when the linear or planar shape factor vanishes. There are three such cases:

1. all three eigenvalues are identical—*isotropic or fully spherical case* at $c_l = c_p = 0$,
2. the major and medium eigenvalue are equal—*fully planar case* $c_l = 0$,
3. the medium and minor eigenvalue are equal—*fully linear case* $c_p = 0$.

The variety of just one shape factor vanishing is larger than both being equal to zero, as is obvious from Figure 9. Zheng and Pang (2004) demonstrated that in generic tensor fields fully linear or fully planar regions occur as connected lines. They also presented a method to determine them. Eigenvector integration methods (e.g., “fiber tracking”) must fail when traversing such regions.¹

The isotropic case is the simplest one in the sense that there is no directional information at all and the tensor is fully described by its trace. Thus, there is no real need for elaborated tensor field visualization methods providing directional information—usual scalar field rendering methods such as gray scale imaging or volume rendering are entirely sufficient. Therefore the authors opted to exclude any isotropic region from the tensor field visualization by setting the transparency of each voxel proportional to its isotropy

¹Such regions are sometimes called “degenerate features of a tensor field.” However, care needs to be taken about the term “degenerate” here: “degenerate eigenvalues” denote multiple eigenvalues, which may or may not be due to multiple eigenvectors. On the other hand, a “degenerate matrix” refers to a singular, that is, non-invertible matrix which does not have full rank. This term is more common for bilinear forms or metric tensor fields. Such a “degenerate tensor” (corresponding to the $c_s = 0$ line in the barycentric shape factor diagram) does not imply “degenerate eigenvalues (which are the $c_p = 0$ and $c_l = 0$ edges of the shape factor triangle), nor vice versa. As can be easily seen at $c_l = 0$ and $c_p = 0$, an invertible (non-degenerate) matrix may possess two different eigenvectors with same (degenerate) eigenvalues (spanning an full eigen space), and a non-invertible (degenerate) matrix at $c_s = 0$ may have three unique (non-degenerate) eigenvalues. Only at the corners with $c_l = 0$, $c_s = 0$ and $c_p = 0$, $c_s = 0$ both flavors of “degeneracy” coincide.

(i.e., the spherical shape factor c_s). Finally, all voxels contained in a user-selected region of interest are rendered back to front, similar to a volume rendering technique known in computer graphics as “splating” (Westover, 1990; Crawfis & Max, 1993). This technique was originally developed for use on astrophysical data sets (Benger & Hege, 2003), but is applicable to diffusion tensor data sets as well (Benger & Hege, 2004). However, in contrast to the classical splating techniques,² here the orientation of the splat elements is fixed in space, not perpendicular to the view plane. As a technical detail but still notable benefit, this property of the rendering technique allows use of OpenGL display lists, thereby achieving fast rendering performance. Still, certain user-adjustable parameters like the airity can be set outside of the OpenGL display list and allow interactive fine-tuning of the image quality.

The third dimension of the color patterns perceptual space, *regularity and placement rules*, is not represented by the graphics primitive itself, but by the entire field: as the Gabor patch itself is maximally regular by construction, variations across various points in the tensor field become obvious. The placement of each pattern element reflects the underlying discrete sampling of data points.

At this point, the most dominant color pattern dimension of *overall color* is yet undetermined and may be used to overlay additional information on top of the spatial pattern structure. In the absence of other priorities it is useful to display the relationship of linearity versus planarity for colorization, because the apparent shape of an arbitrarily oriented two-dimensional ellipse (and thus the Gabor patch) in three-dimensional space is ambiguous.

Colorization

For inspecting DT data sets for medical analysis the absolute velocity of water diffusion may play an important role. The technique of “tensor splats” in its original form employs normalized icons and does not provide information about the absolute velocity, that is, the trace of the tensor field. It is possible to scale the geometry of the splat elements to reflect the size of the corresponding (unnormalized) ellipsoid, but this approach results in a unpleasant, discontinuous appearance of the entire image. What is left over from the perceptual dimensions of color patterns (see p. 484) is the *color purity*. So the original technique of “tensor splats” was extended to incorpo-

²Including the similarly named method of “tensor splating” (Bhalerao & Westin, 2003).

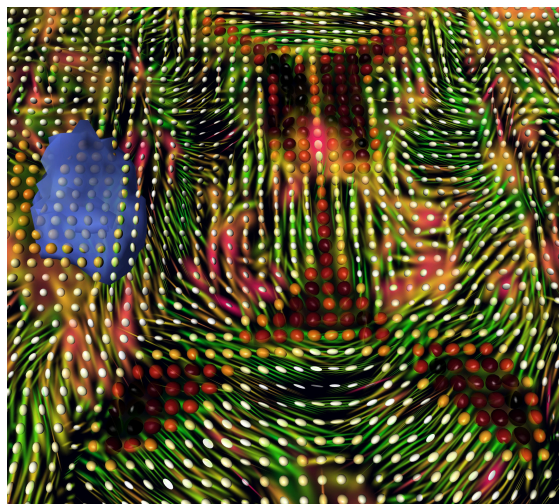


Figure 15. Detailed view of the coincidence of tensor ellipsoids and tensor patterns. (See Color Plate 37 at end of issue.)

rate displaying the trace of the tensor via saturation of the colors. This fixes (or at least limits) the choice of colors and one has to consider perceptual pattern-color interactions. As Poirson and Wandell (1996) point out, three separate neuronal pathways coexist within a single region of the visual field, and each pathway has different pattern sensitivity.

The visual sensitivity of spatial patterns depends on the color, mainly (more than 50%) due to the chromatic aberration within the human eye (Wandell, 1993). Although the highest sensitivity is maintained for black and white patterns, this option is not available when intending to incorporate saturation in the model. The red-green sensitivity is noticeable larger than the blue-yellow sensitivity at spatial frequencies of up to eight cycles per degree (8 cpd). This is the range where people still have good color and contrast vision. A spatial frequency of 10 cpd roughly corresponds³ to a detail at the size of three pixels on a 17" screen of resolution 1280×1024 when viewed from a distance of 20". So for inspecting an information-rich image at high resolution, a red-green contrast is the preferred choice.

³Diagonal 1700 is approximately $\sqrt{1280^2 + 1024^2}$ pixel, makes 100 pixels per inch on a 17" screen, that is, 100 dpi. Seen from a distance of 57", one degree is exactly one inch, as one radian is 57°. These are 100 pixels. From a third the distance, ca. 20", one degree covers 30 pixels and a tenth corresponding to 10 cpd results in three pixels.

Table 2. Summary of the mapping of the six independent tensorial quantities to the rendering quantum

Tensor quantity	dof	Graphical representation
Max. EV (normalized)	2	Major orientation of Gabor patch
Med. EV (perpendicular, normalized)	1	Minor orientation of Gabor patch
Isotropy (sphericity)	1	Transparency
Planar vs. linear	1	Spatial frequency and red/green trace
	1	Saturation
Full tensor	6	Tensor pattern

dof = Degrees of freedom.

The result is a pattern-like overview to provide a smooth, contiguous view (see Figure 15 for comparison with usual ellipsoid rendering) of an entire data slice, as exemplified in Figures 21, 22, and 23, or even volumetric region, as in Figures 24 and 25. The mapping of the six independent tensorial quantities to the rendering quantum may be summarized in Table 2.

As the eye usually accommodates for its most sensitive wavelength around 580 nm, it is moreover canonical to colorize the crisp patterns occurring in linear regions in green and leave red to the more fuzzy planar regions. Finally it is noted that a linear blend of red and green yields unpleasant brown. Using an asymmetric, nonlinear blend function allows passing through yellow during color transition. With yellow being the perceptually brightest color of the spectrum, there is a means to specifically enhance a certain threshold among linear and planar regions. This choice of colorization leaves blue free for use in a background image map, which is useful to allow orientation in the data sets. This color scheme was used in Figure 22 (upper left), 23 (upper right) as well as in Figure 26, 27, 28, and 29, all shown later in the article.

Tensor Legend

To demonstrate the mapping of tensorial quantities to icon parameters and build an intuition of the graphical representation of the tensor field, the authors conceived an artificial tensor field to serve as a legend for the graphics primitives. Its purpose is to show variations of the shape parameters along the edges of nested triangles of constant tensor trace. The size of the triangle corresponds to the tensor trace. Only variations of the extreme cases are shown, such that at each point at least one shape factor vanishes. Consequently, the outline of each triangle follows a one-dimensional periodic pa-

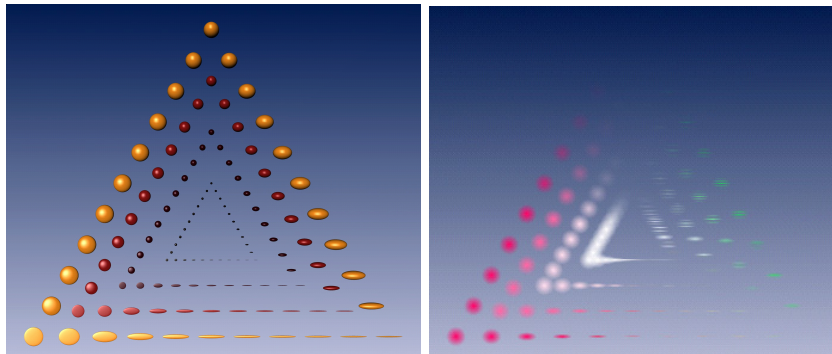


Figure 16. Including variations of trace in the tensor legend via nesting of shape factor triangles, whereby trace is kept constant per triangle. (*Left*) Normalized quadric surfaces (trace indicated by color instead of size). (*Right*) Tensor patterns with saturation set proportional to tensor trace. (See Color Plate 38 at end of issue.)

parameterization. Together with tensor trace as radial parameter this tensor field covers a plane and is suitable as a legend.

Figure 16 demonstrates locations in a tensor field of constant trace, forming nested triangles. Because the authors are interested in visualizing large tensor fields of many tensors with known regular structure, they also tested the tensor legend field sampled on random locations. The generating scalar fields of trace and shape factors on these random locations are shown in Figure 17. Dark areas in the shape factor images depict the sections where the respective shape factor vanishes. Note that eigenvector streamlines are completely undefined in fully planar areas, that is, the dark section in the upper left of the third image. Figure 18 applies iconic techniques to the tensor legend field. Direct rendering of tensor ellipsoids directly maps the tensor quantities,

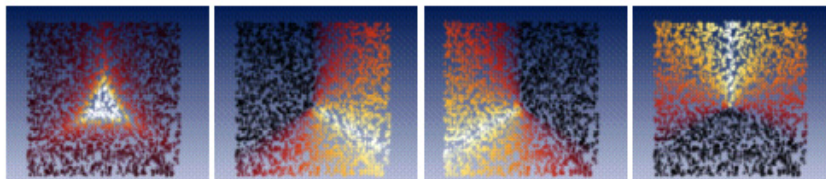


Figure 17. Shape factors on 2,500 randomly distributed locations in a barycentrically parameterized artificial tensor field: trace, linearity, planarity, and sphericity. At each point, one of the shape factors vanishes. Concentric triangles represent variations of all shape factors for constant trace. (See Color Plate 39 at end of issue.)

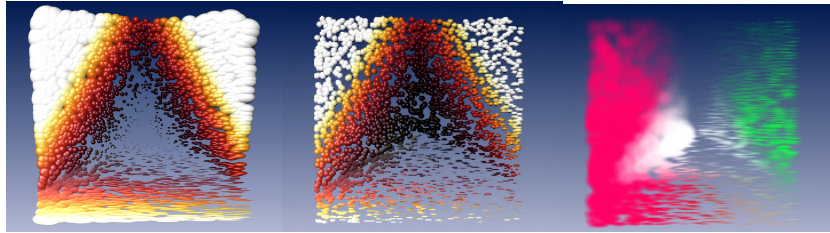


Figure 18. Tensor visualization of 2,500 randomly distributed locations in a barycentrically parameterized artificial tensor field: Quadric surfaces (*left*), normalized ellipsoids (*center*), and saturation-valued tensor patterns. Intense colors correspond to high tensor trace, that is, high diffusion probability and low diffusion coefficient. Tensor patterns are very sensitive to fine variations of the tensor shape, but still provide a homogeneous display of the entire data set. (See Color Plate 40 at end of issue.)

but is problematic due to its large variations of ellipsoids leading to severe view occlusion problems. Normalizing the ellipsoids to the same size cures this problem, but variations in tensor shape are hardly perceptible. Tensor patterns are regularly defined over the entire field and display even fine variations in the tensor field in an intuitive way. Also, due to their transparent nature, tensor patterns may also be employed in a three-dimensional volume, as demonstrated in Figure 25, later in the article.

APPLICATION TO DATA SETS AND TUMOR ANALYSIS

Medical Demand on Tumor Visualization

Neuroepithelial Tumors—Overview. Gliomas arising from cells derived from primitive neuroepithelium constitute the most important group of intracranial tumors. Classifications are based on the histology of the neoplastic tissue. They focus on the identification of precise cytological features linking neoplastic elements to normal cell types found in mature and developing central nervous system. First Bailey and Cushing (1926) attempted to classify the tumors observed in terms of the different morphological stages through which these cells pass in ontogenesis (Bailey & Cushing, 1926). The World Health Organization (WHO) ratified in 1993 a comprehensive classification based on a separation of tumors of neuroglial cells from those of neuronal origin or composed of primitive bipotential precursor cells with the latter being able to differentiate along divergent glial and neuronal lines (Kleihues et al., 1993).

Since descending from an abnormal growth of a specific cell type the behavior of the tumor type correlates with basic cell type in a certain relation. The extent dictates the choice of therapy and predicts prognosis. The WHO categories do provide a parallel grading system (WHO grades I to IV) for each type of tumor with most named tumors being of a single defined grade. Astrocytic or glial tumors are subdivided in *pilocytic astrocytoma* (WHO grade I), *astrocytoma* (WHO grade II), anaplastic (malignant) *astrocytoma* (WHO grade III), and *Glioblastoma multiforme* (WHO grade IV). Not included in the WHO classification, tumors can be subclassified as invasive or non-invasive.

There is a high diversity of cellular morphology of brain tumors. The complexity of gliomas is due to the considerable cell types involved. Anaplasia describes the reversion of cells to an immature or a less differentiated form. This is to be detected in glial neoplastic tissue as a developmental process. The more primitive condition results in the alteration in cell character, which constitutes malignancy. Moreover, there is evidence of a horizontal transformation of malignancy from the initial neoplastic cell population to putatively normal stromal cells resulting in a transfer of genetic information coding for malignant change. Variations of tumor structure are found both within the classes of gliomas as well as in the different sections of an individual tumor (Berry, 1988). The aforementioned tumor characteristics challenge the diagnostic and therapeutic approaches.

Modern brain tumor therapy consists of a combination of surgery, radiation, and, chemotherapy. Although discussed controversially the preferably radical resection of brain tumors (“cytoreduction”) still represents the therapeutic method of choice (Ciric et al., 1987; Kiwit et al., 1996; Scerrati et al., 1996). Because tumors grow in the restricted space of the skull, progressively involve neighboring structures with a subsequent functional adverse effect, feature an increasing malignant potential, and, at least because non-interventional therapeutic methods like chemotherapy or radiation only provide minor immediate effects, the maximal surgical reduction of neoplastic tissue is an essential procedure to achieve a preferably long survival time. To reduce postoperative morbidity eloquent structures are spared under the assumption of tumor tissue remains. This approach is appropriate because the complete reduction in principle is impossible due to the tumor biology and the infiltrative growth.

Conventional MRI of Brain Tumors. The aim of the diagnostic imaging using conventional MR technology is the appraisal of tumor dignity and

preoperative characterization of the topographic relationship between the tumor and eloquent structures of the brain parenchyma. Tumor visualization relies on the more or less delineated signal change in conventional T_2 - and T_1 -weighted sequences (signal increase in T_2 and signal reduction in T_1) compared to normal brain parenchyma. The signal distinction is a result of changed local cell density and cell composition of the tumor tissue.

The increase in cell numbers (hyperplasia) of the tumor tissue results in an increased volume of the infiltrated brain structures and a displacing mass effect. Aggravating the detection commonly perifocal edema blurs the edge between the tumor-infiltrated brain tissue and neighboring edematous parenchyma. There is no conventional method that clarifies the change from tumor to perifocal edema. Magnetization prepared T_2 -weighted sequences suppressing the free liquid signal (FLAIR; Fluid Attenuated Inversion Recovery) better allow to delineate pathologically changed areas from cortical structures and cerebrospinal fluid containing compartments. However the exact distinction of tumor tissue from perifocal edema is not sufficient. The neoplastic neovascularization entails a break-down of the blood-brain-barrier (BBB). This leads to a pass over of applied contrast agents into tumor tissue detectable at T_1 -weighted sequences. Increasingly disintegrated tumor fractions show a signal isointens with cerebrospinal fluid at all conventional MR sequences representing a central necrosis.

The derivation of gliomas from matrix forming cell types of the central nervous system determines the primary localization in the brain white matter and the high affinity of spreading tumor tissue to fiber systems. This spread is detectable as a signal change along anatomically known fiber tracts and fascicles in conventional MR sequences. Depending on the degree of malignity of the regional tumor tissue this results in an infiltration of fiber systems without a functional adverse effect as far as a primary destruction causing a loss of function. The underlying mechanism and the extent of destruction inevitable leading toward a loss of function are unidentified.

Diffusion Tensor Imaging of Brain Tumors. Current routine imaging techniques are incapable of depicting the white matter tracts. The quantifiable imaging method Diffusion Tensor MRI is sensitive to microscopic motion of water. It provides a quantitative measure of restricted free water diffusion in highly organized tissues. Because diffusion in brain white matter fiber structures is directionally dependent this method maps the degree of directionality of white matter pathways and consequently its aberrance under pathologic conditions. Thus, Diffusion Tensor MRI has a potential to assess disease states of cerebral white matter.

Behind the basic scientific identification of the functional organization and neural connectivity a highly demanded clinical application exists with an prompt impact on an individual patients health—the detection of eloquent, that is, vitally important white matter structures that should be spared by neurosurgical procedures. It is necessary to depict a tumor within its white matter environment. The more accurate the imaging of a brain harboring a malignant tumor the more precise local resection or sparing of eloquent fiber structures is feasible.

White matter tract visualization allows neuroradiologists to provide relevant interpretations about the actual state on the basis of a simple morphologic analysis of the neuronal network. Although DTI reveals displacement, edema, infiltration, and, disruption of fibers adjacent to tumor tissue (Witwer et al., 2002). It is assumed that abnormal-appearing white matter although can contain anatomically intact fiber systems.

However, there is no preoperative method to specifically characterize the interaction between tumor tissue and white matter fibers. Although white matter tractography and eigenvector color maps present visual displays of white matter tract organization, the quantitative and statistical analysis of diffusion characteristics is mandatory. Field et al. (2004) categorized the varied appearances of tumor-altered white matter tracts on a combination of the apparent diffusion coefficient, the fractional anisotropy, and the major eigenvector direction. Infiltrating tumor was found to produce tensor directional changes that were not observed with edema. Recent research goes beyond the measurable magnitude, anisotropy, and orientation of water diffusion of brain tissues in DTI data. Price et al. (2004) categorized displaced, infiltrated, and disrupted white matter tracts by a combination of the analyzed isotropic and anisotropic components of diffusion. Wu et al. (2004) used rose diagrams, which are spherical coordinate histograms of the major eigenvector directions, 3-D scatterplots of the major eigenvector angles, matrices of major eigenvector directions to describe the distribution of major eigenvectors, and a measure of eigenvector dispersion to describe the degree of eigenvector coherence and the interhemispheric symmetry. They found infiltrative diseases to alter the eigenvector properties of affected white matter tracts, showing a decrease in both characteristics.

Data Acquisition and Expectations

Data Acquisition. DT-MRI images were acquired on an 1.5T MRI scanner (Sonata, Siemens, Germany). A set of DWIs was obtained by using a diffusion weighted spin-echo EPI sequence. Measuring parameters were as follows:

FOV = 23×23 cm, matrix = 1282, slice thickness 3 mm, TR = 3700 ms, TE = 85 ms, NEX = 8, b-value = 1000 s/mm^2 . A reference image at $b = 0$ as well as six diffusion weighted images (for the tumor patient) (gradient vectors as follows: (1,0,1), (-1,0,1), (0,1,1), (0,1,-1), (1,1,0), (-1,1,0)) with a b-value of 1000 s/mm^2 were taken.

The T_1 -weighted 3-D image was acquired with TR = 1900 ms, TE = 4.38 ms, TI = 1100 ms, NS = 1, on a matrix of 512^2 with slice thickness of 1 mm. The 3-D- T_2 -weighted fluid suppressed sequence used TR = 6000 ms, TE = 354 ms, TI = 2200 ms, on a matrix of 256×232 on a slice thickness of 1 mm as well.

For a healthy volunteer a data set of twelve gradient measurements was also acquired, which was used to test the statistical analysis tools. Due to clinical constraints, the authors were not able to perform the statistical tests on the tumor patient.

Patient Information. The dataset of a brain harboring a tumor was derived from a 28-year-old female. She had a two-year-history of brachio-facial seizures before neuroimaging was applied. It revealed a tumor consistent with an astrocytoma. Primarily located in the right insula it shows a close relation to the posterior limb of the internal capsule. This fiber structure contains the corticospinal tract that mediates the primary motor action.

Subsequently the patient underwent neurosurgical therapy without resulting complications or postoperative neurological deficits. The tumor was histologically identified as a fibrillary astrocytoma consistent with a WHO grade II variant.

Expectations. DTI has a clinical implication in that this technique may detect changes of integrity of white matter adjacent to brain tumors. This is an important issue because preserving vital cerebral function while maximizing tumor resection is the main aim of neurosurgical therapy. During conventional operating techniques the detection of tumor extent is based on the visual and tactile impression of the neurosurgeon (see Figure 19) and the deduction of the location of eloquent areas from general anatomic knowledge. Both practices are aggravated when at least low-grade gliomas are visually undistinguishable from unaffected brain tissue or if eloquent areas are displaced by mass effect or infiltrated. A more specific imaging to illustrate the tumor relation to subcortical structures is needed identifying tumor infiltration. This should support maximizing the tumor resection or the total resection if possible in early stages of neoplastic disease. A more accurate



Figure 19. Intraoperative microscopic view on the right insular partially resected tumor, image courtesy by G. Schackert, M.D. The same tumor is displayed as in the datasets in Figure 2 and following. The image is a fragment of a screenshot of a navigational system routinely used to display operative instruments registered in space in a preoperative 3-D MRI scan (BrainLAB VectorVision Cranial, Heimstetten, Germany). Note that there are no significant differences of the tumor and brain parenchyma appearance in terms of color. (See Color Plate 41 at end of issue.)

preoperative delineation of tumor location will provide a better prediction of clinical outcome.

Taking into account the spatial resolution of MR scans of about 1 mm and the diameter of a typical axon of about 1 μm , it is quite clear that the data resolution is far too coarse to provide means of tracking single, densely packed axons. In regions where many axons run in parallel, a visualization technique can thus just try to render this situation symbolically. In other regions, where axons may run in different directions within a voxel, trying to seriously track single fibers is futile, especially taking into account noise (see discussion in “Quality Measurements for the Tensor Fit”) in the acquired data, uncertainties due to the chosen interpolation method (see “Interpolation of Tensor Fields”) and the resulting inherent instability in following the principal direction of the diffusion tensor field.

The visualization approach described in “Visualization via Color Patterns” distills the comprehensive 3-D information available from the diffusion tensor field without suggesting higher precision than actually available in the data. The technique of tensor patterns as a purely vertex-based approach is inherently independent from a choice of interpolation method while

still providing smooth images. It does not claim to provide an exact tool for tracking fibers, but the shown method is expected to give a more accurate insight into the interaction between tumor and white matter. To prove the potential requires further systematic study on clinical data.

DISCUSSION

Observed Diffusion in the Tumor Tissue

Relatively compact glia cells that are constantly dividing, growing, and thereby subsequently oppressing the surrounding tissue form tumor tissue. Tumors usually do not contain axon fibers, which would contribute to diffusion anisotropy, unless they infiltrate white matter fiber structures. Therefore it was expected that the region of tumor would show high isotropy in the diffusion tensor field as compared to the white matter. This behavior is clearly depicted by the visualizations. The increase in extracellular space as reported by Bruehlmeier et al. (2003) and Vargova et al. (2003) is probably the cause of the observed higher diffusion rate.

Partial Volume Effects. There are reasons to suspect the model of a tensor of rank two per volume element to be insufficient. The limited spatial resolution of the diffusion measurements results in averaged diffusion measurements across finite regions in the tissue and thus the assumption of a simple diffusion tensor of rank two may be incorrect, that is, tensors of higher rank are required that are able to incorporate the contributions from unresolved microstructures. Especially in regions where there are crossing axonal fibers one can suspect that a 2nd order model is misleading (Wiegell et al., 2000). There have been multiple models introduced in order to extend the model of a quadratic form for the diffusion process. Using a large number of gradient measurements (Tuch et al., 1999) introduced high angular resolution diffusion imaging. Özarlan and Mareci (2003) introduced the fit of higher order tensors in a large number of gradient measurements. Those methods require in the order of 80–100 gradients, which are equally distributed around the half-sphere. Because of the low number of gradient directions (12) in the current experimental setup the authors did not attempt to learn a more complicated model. But it is argued that additional gradient direction measurements can be used to validate the 2nd order model. For this reason a measure for the fit of the tensor model to the diffusion signal was introduced.

Figure 20 shows results for both statistics, the modified Bingham statistic, which can be used to give confidence regions for the eigenvalues of the

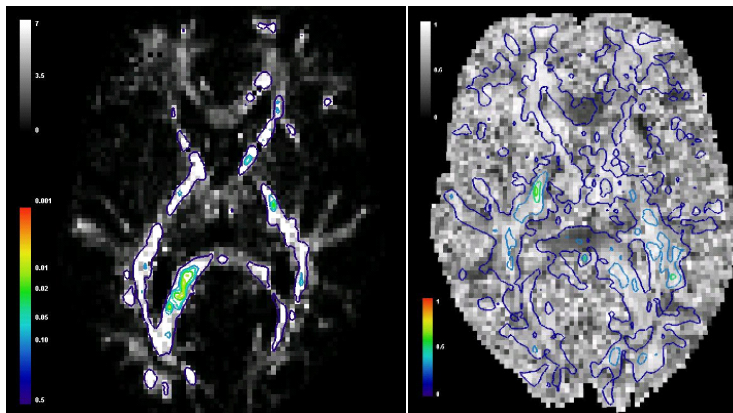


Figure 20. Bingham statistics and correlation coefficient for a single slice, dataset of a healthy patient. Left: The value of the Bingham statistic per voxel in a single slice. Values are drawn according to the top legend. The iso-lines represent areas for which with a specific probability the hypothesis of isotropic diffusion can be rejected. For the probabilities the values listed in Table 1 were used. Right: The corresponding values for the correlation coefficient with additional isolines for different levels of the linear measure $c_l(0, 1)$ according to the color legend. (See Color Plate 42 at end of issue.)

tensor (reject the hypothesis of isotropic diffusion) and the correlation coefficient between the 2nd order tensor model and the measured values. The results for the Bingham statistic are weak and reflect the low number of measurements used in this data sample (12 gradient directions). The eigenvalues can therefore be trusted only for very few voxels at a probability level of 0.1.

The values for the correlation coefficient are all positive, which is expected because the second-rank tensor was obtained as a fit to the measured values. The correlation coefficient shows some spatial features that remind of regions in the diffusion tensor field with primarily one dominant diffusion direction (compare with Figure 10). A possible relationship was tested by comparing the linear measure c_l [as defined by Eq. (12)] of the diffusion tensor to the quality of the model fit expressed as its correlation coefficient (see isolines in Figure 20 right). The correlation coefficient for brain regions with a c_l value higher than 0.3 is 0.76 ± 0.11 whereas for regions with low anisotropy (<0.3) it is 0.62 ± 0.16 . Both are not significantly different and therefore the data does not indicate a better model fit in regions of large anisotropy in the data. This indicates that even in regions of large anisotropy

in the data a significant part of the diffusion is measured orthogonal to the principal diffusion direction.

In conclusion it was found that measuring six diffusion gradients only cannot bound the error introduced in the measurements by noise. It was also found that 12 diffusion gradients measurements are not sufficient for a statistically significant 2nd order tensor fit in most regions of the white matter. It is expected that the statistics can be improved by using more measurements, which is especially important for a future use of the diffusion tensor method in medical diagnostics.

Visual Data Inspection. The diffusion data set was available at a spatial resolution of 2 mm. The tensor patterns technique displays the data as-is, with no inherent artificial data interpolation. The authors prefer this visualization approach because otherwise visual results would also depend on the used interpolation method and not merely on the data. A strong example of the influence of interpolation method on visual results is shown in Zheng and Pang (2004). However, although the visualization methods display some indication, for detailed data analysis of the interaction of the tumor and the surrounding tissues the available resolution appeared to be too low and the authors experimented with artificially interpolated data. The results show the potential of diffusion tensor data acquired in higher resolution, but currently have to be interpreted with care.

Unfortunately, enhancing the resolution of the diffusion tensor data results in a higher signal-to-noise ratio, as there are fewer protons available per voxel. Consequently the data acquisition times need to be increased. However, the acquisition of the used data set already required ca. 10 minutes, which is at the toleration limit in a practical environment. With measuring times of up to 8 hours, it was possible to achieve a spatial resolution in the area of a few dozen microns, but this option is unrealistic for clinical use on patients. An alternative was to decrease the field of view or to increase the strength of the magnetic field. Whether any of these approaches might be feasible, awaits further investigation.

CONCLUSION

This article has presented a novel method for visualizing symmetric tensor fields of rank two and a new statistical analysis tool for quality assessment of diffusion-weighted magnetic resonance image data.

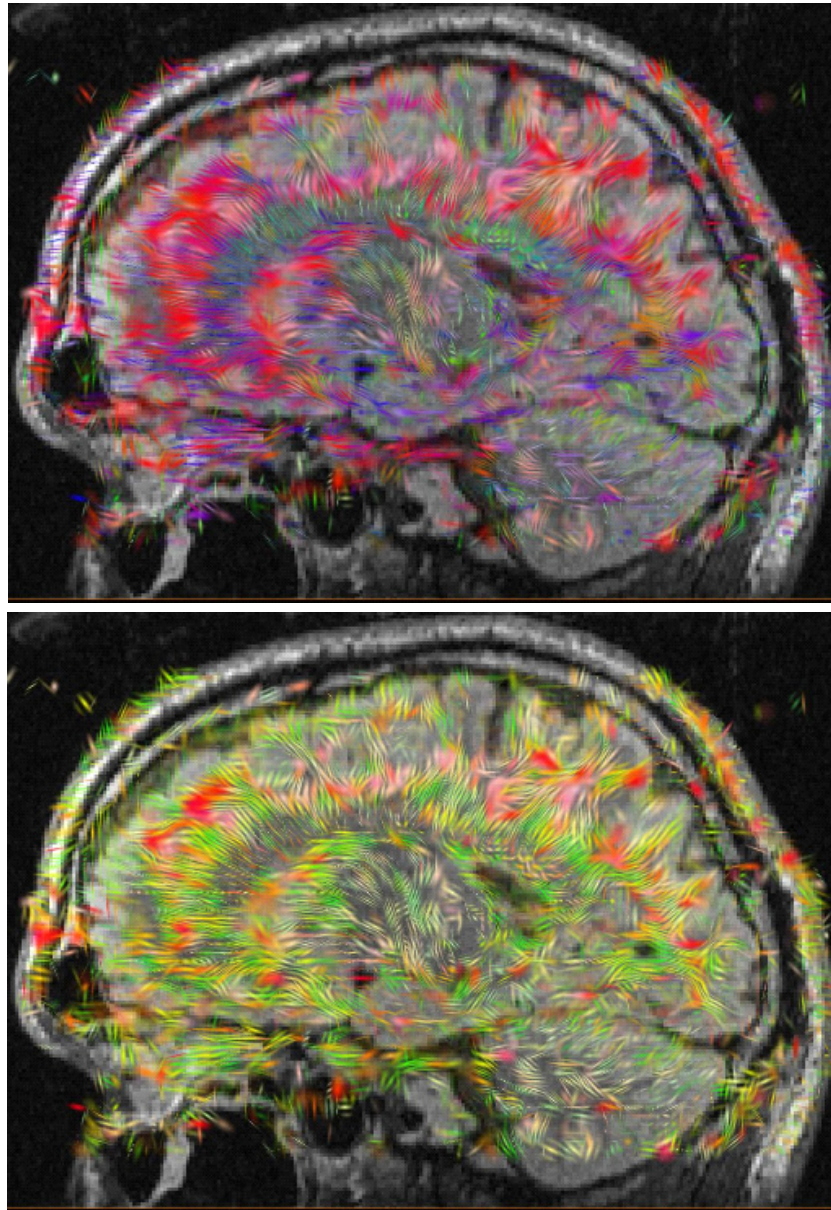


Figure 21. Diffusion tensor field of an healthy patient's brain. Directional color map (*upper image*) and linearity vs. planarity colorization (*lower image*). Pale colors indicate high diffusion velocity. (See Color Plate 43 at end of issue.)

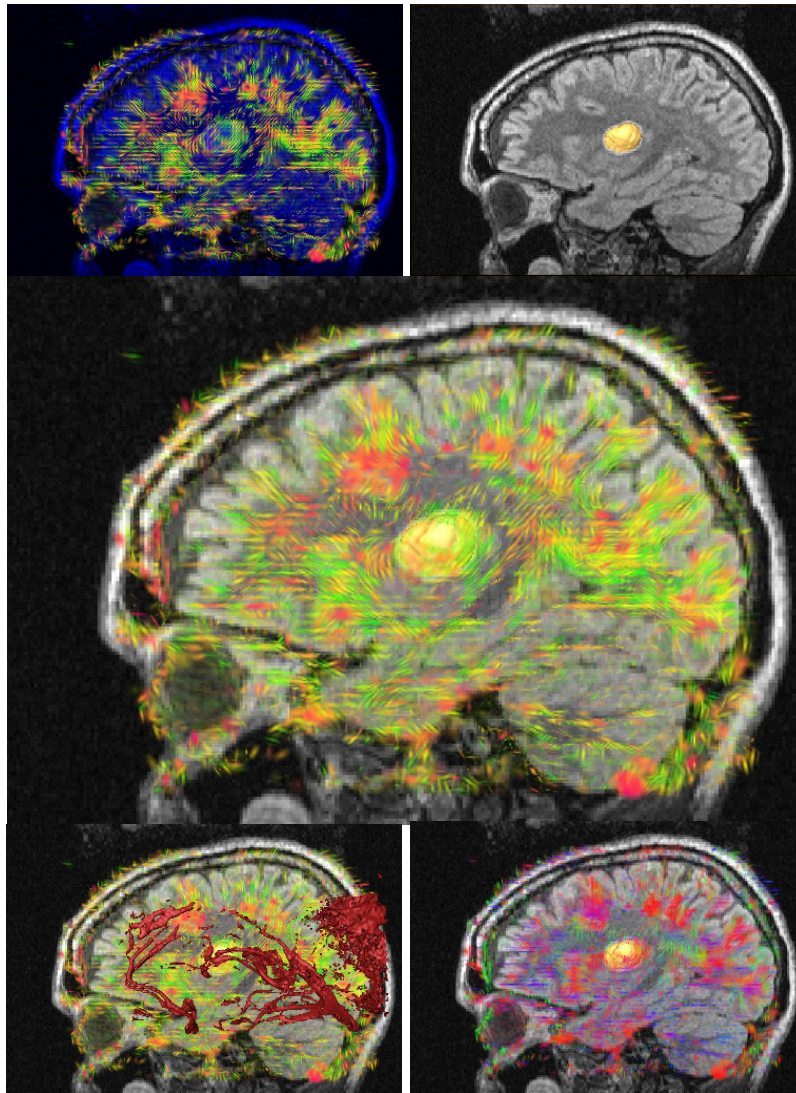


Figure 22. Variations of rendering a sagittal slice from the same dataset as in Figure 2 in medial view (see Figure 24 for three-dimensional overview). The tensor patterns can pretty well be overlaid with conventional imaging techniques to support physicians finding known structures. The yellow knob is a three-dimensional isosurface of the tumor as determined from the T_2 image data (*upper right*), but it is visible in the tensor data as well (*upper left*). There is evidence of fiber structures within or traveling out of the tumor, as indicated by the green, linear patterns. See also Figure 23 for further explanation. (See Color Plate 44 at end of issue.)

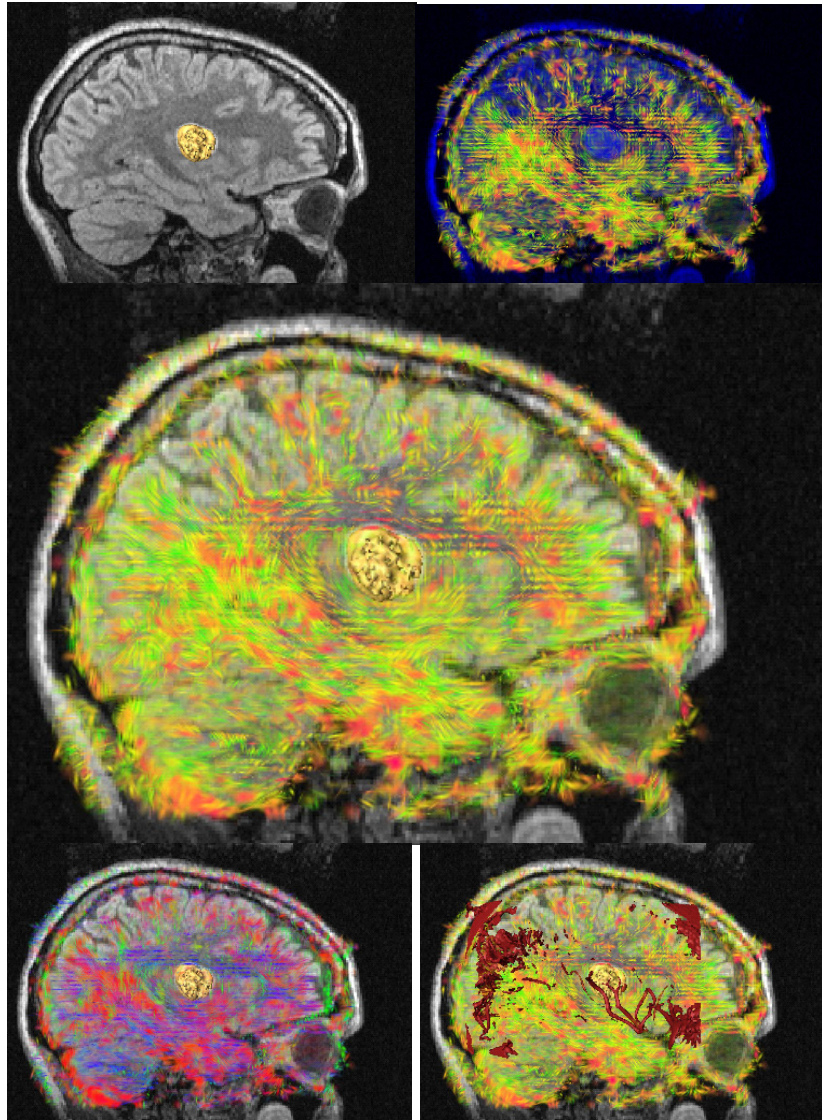


Figure 23. Same arrangement as Figure 22, but lateral view. The diffusion tensor field provides information primarily in areas where the conventional T_2 image (*upper right*) appears homogeneous. Whereas the tumor is smooth on the inside and covered by linear neuronal fibers of the posterior limb of the internal capsule (Figure 22), it is structured more complex on the outside. The lower left image employs color-coding of the maximum eigenvector. Although this colorization enhances areas of similar diffusion direction, it hardly indicates planar regions, that is, fiber crossings. (See Color Plate 45 at end of issue.)

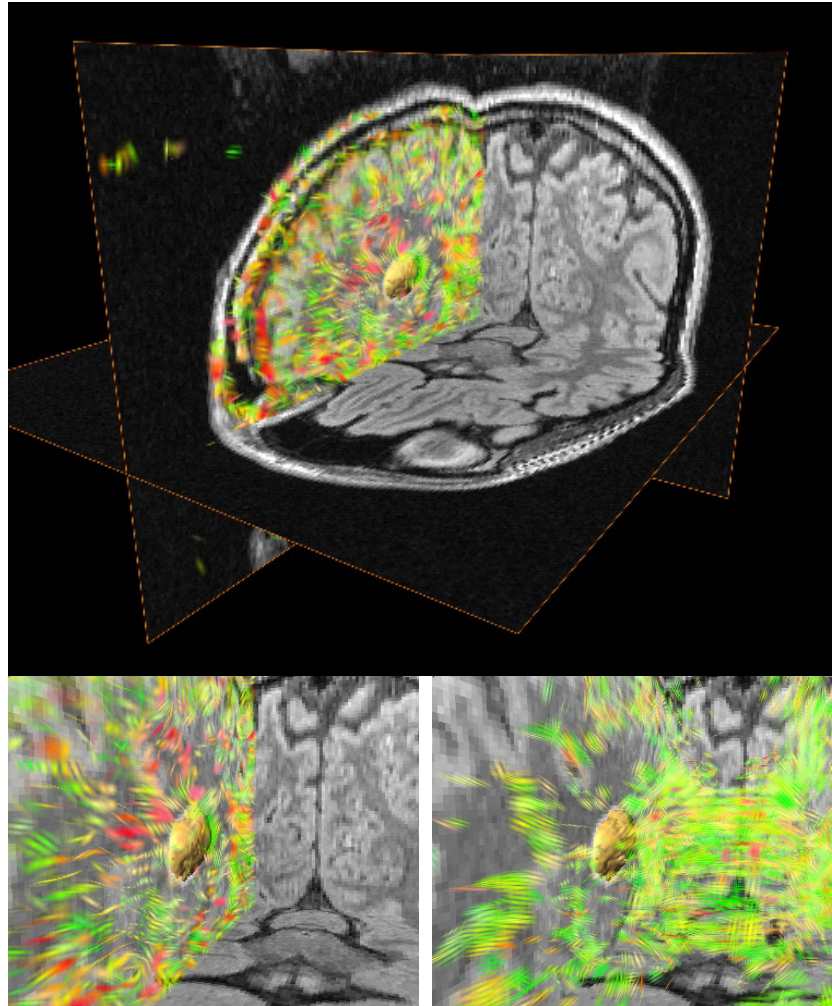


Figure 24. Three-dimensional view of a brain octant from the Figure 2 dataset, with zoom and demonstration that “tensor patterns” can also be used in a volume; they are not limited to slices. However, usually the display settings need to be adjusted differently. Actually all tensor patterns are three-dimensional objects by themselves. Consequently, in the zoomed image, some evidence of fiber structures of linear diffusion traveling in and out of the tumor (yellow surface) may be seen. If this is consistent with tumor infiltration awaits further investigation. (See Color Plate 46 at end of issue.)

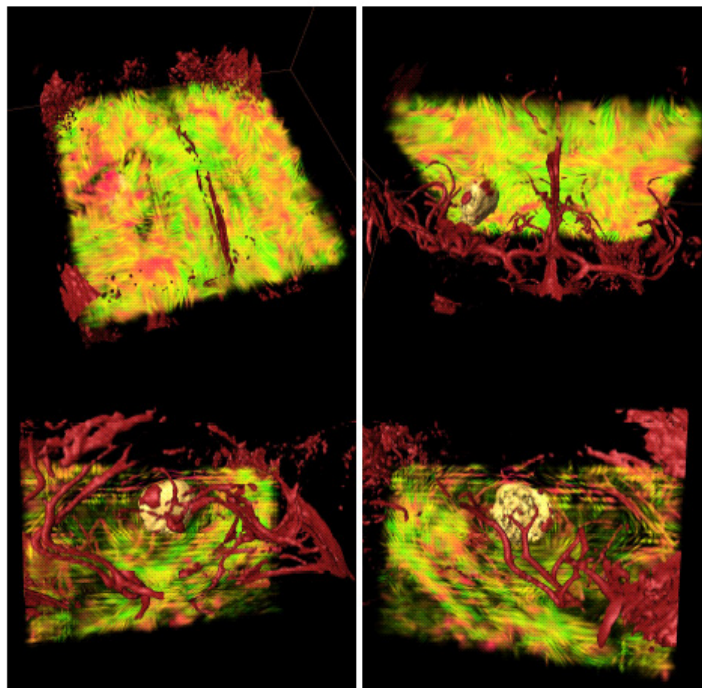


Figure 25. 3-D view of a volumetric region of the Figure 2 data visualized with tensor patterns together with blood vessels (dark red), which have been extracted from T_1 at value 100. Vessels are visible in the T_1 image due to an injected contrast medium; consequently, contrast-enhancing regions in the tumor appear as well. This approach illustrates arterial and venous vessels similarly. The red area in the tensor patterns above the tumor (*upper left*) indicates planar diffusion. In the sagittal view (*lower row*) the diffusion tensor patterns display the pressure of the tumor on the surrounding tissues. (See Color Plate 47 at end of issue.)

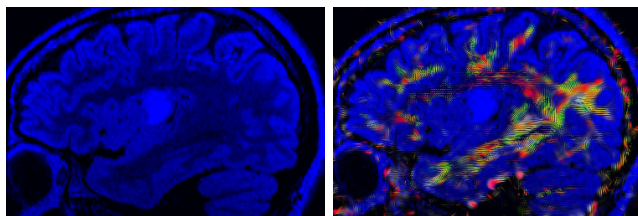


Figure 26. T_2 image from data as in Figure 2, and overlay with very transparent tensor patterns. The tensor patterns' visualization parameters can be adjusted interactively to reveal a sparse or dense display of the diffusion structure. This is of certain importance because the diffusion tensor field particularly provides structural information where the conventional MRI appears widely homogeneous. The T_2 image data was rendered in blue here because this color is not used for tensor patterns and whitish is required for desaturated colors. (See Color Plate 48 at end of issue.)

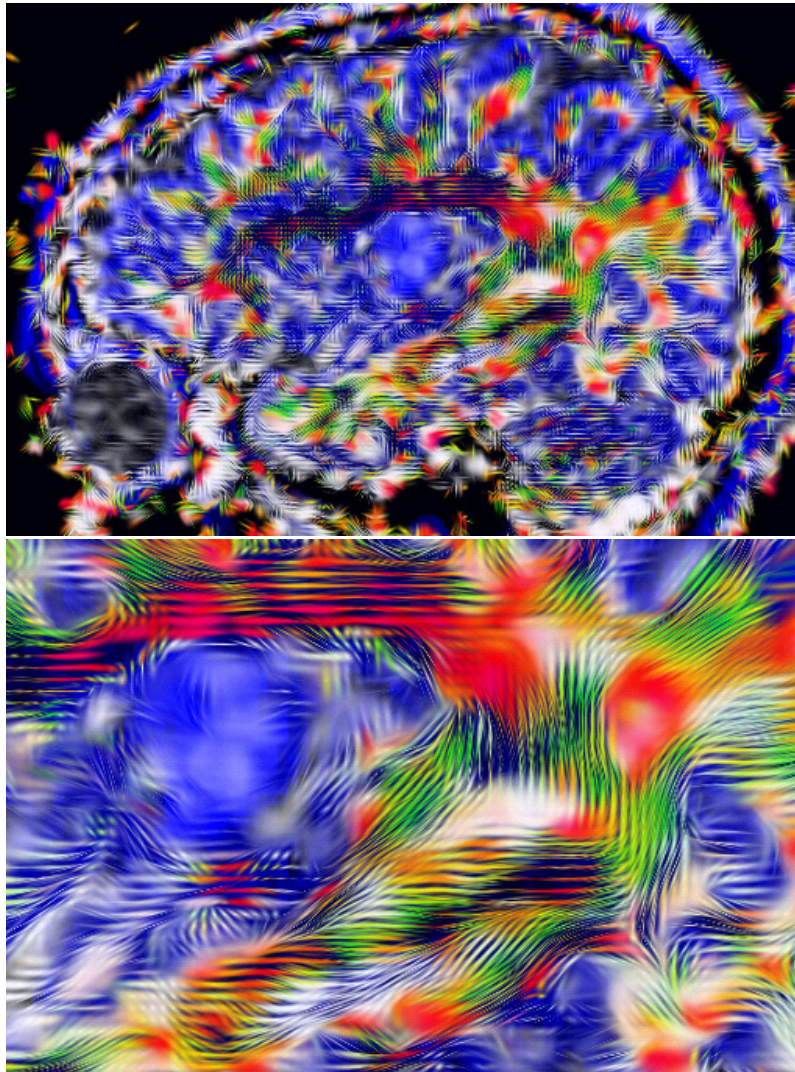


Figure 27. T_2 image (blue), overlaid with tensor patterns (same as Figure 26, but denser setting), and zoom into relevant region. The flow pattern was computed on an interpolated grid of twice the originally measured resolution. It demonstrates the smooth, continuous view of the diffusion tensor patterns with merging of linear areas to planar ones. The net effect is similar to integration lines, but no integration is performed here and no eigenvector ambiguities harm visually or numerically. Moreover, regions of fast (highly saturated colors, especially within the tumor) and slow diffusion (pale colors) are easily perceptible. The tumor moreover appears transparently in the patterns, indicating its high isotropy. (See Color Plate 49 at end of issue.)

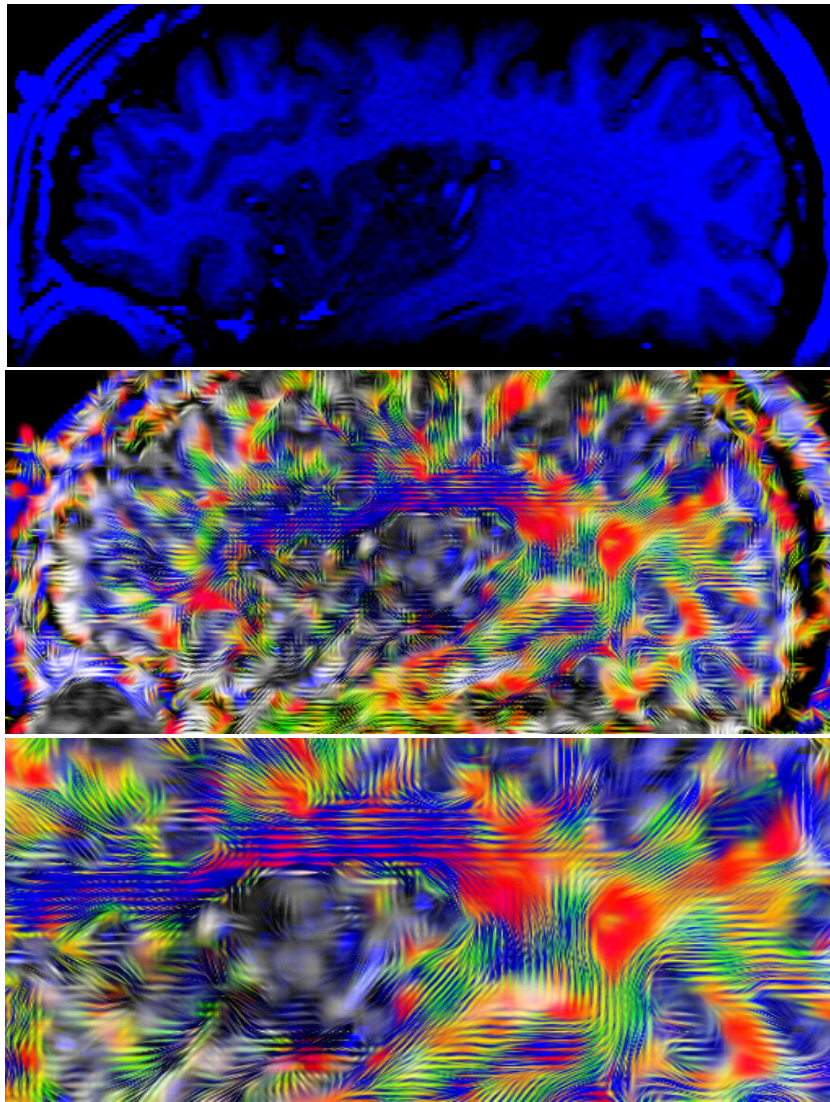


Figure 28. Overlay of diffusion tensor patterns and the T₁ image data, same dataset as in Figure 2. Similar as with the T₂ image, the diffusion data primarily show structure where the T₁ image appears homogeneous. Still, we see strong coincidence of the structures depicted by T₁ and the diffusion field is seen. (See Color Plate 50 at end of issue.)

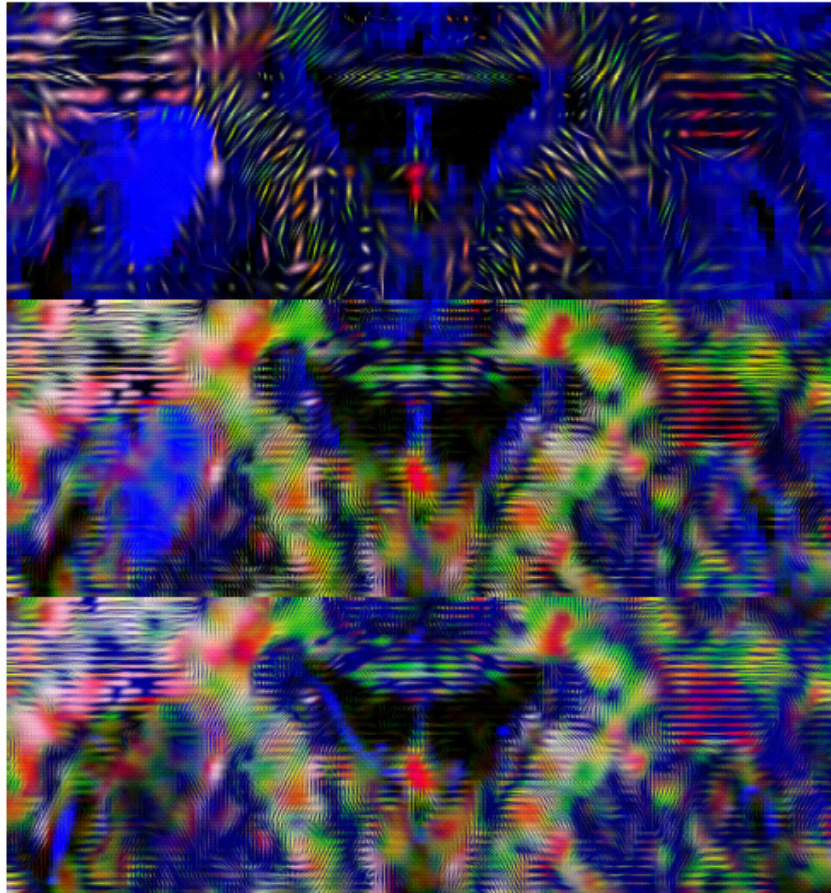


Figure 29. Interaction of the tumor with the surrounding tissues, using same dataset as in Figure 2. The measured data (*top image*) were interpolated using the Lanczos algorithm to four times the resolution, which corresponding to the detail available in the T_1 image. The T_2 image is used in the background, colored in blue. The bright blue appearance of the tumor in the T_2 image underlies a more or less isotropic area in the diffusion tensor. The center image displays tumor tissue spreading onto the lateral surface of the internal capsule presented by linear diffusion depicted by green linear patterns. If this is consistent with an infiltration awaits further investigation. The structures visible in the T_1 image matches with the diffusion patterns within the tumor, depicting flow around a region with contrast medium. However, the reliability of interpolated data (see also Figure 30) is limited. Nevertheless the potential of data that were available in higher resolution is seen. (See Color Plate 51 at end of issue.)

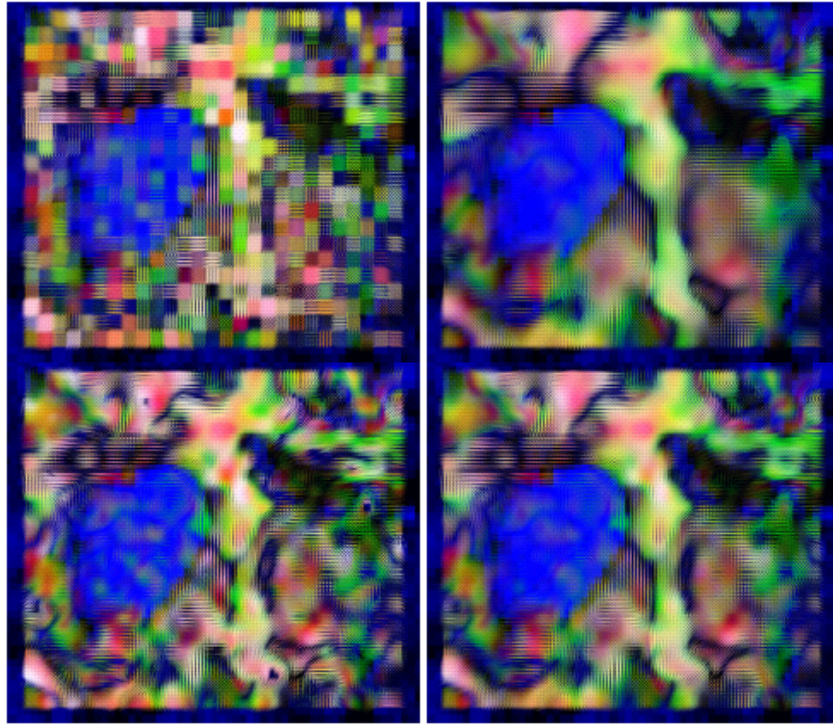


Figure 30. Influence of interpolation demonstrated via comparison of various schemes: nearest neighbor (*upper left*), B-splines (*upper right*), Lanczos (*lower left*), and Mitchell (*lower right*) algorithm. Clearly, the patchwork of the nearest neighbor scheme, shown here for demonstration purposes, is unusable for integration purposes. However, the influence of the smoothing algorithms on the interpolated data is also significant and will influence integral lines (fiber tracking). The B-spline interpolated image hardly shows any overlap of the tumor region with linear fibers. The Lanczos interpolation, similar to cubic, shows such feature, but does not sustain the positive definiteness of the tensor field, thus is questionable. The Mitchell interpolation, similar to linear interpolation, visually appears best. (See Color Plate 52 at end of issue.)

Preliminary results indicate that in general a diffusion model of just second order is insufficient. Sensitive features extracted from the second-order tensor model such as the maximal eigenvector have to be critically examined for their reliability. The trustfulness of visualization methods that are based on such sensitive features has thus to be questioned.

The described visualization technique is supported by neurophysiological considerations on the perception of color-patterns. It is able to display all tensorial quantities in a selected spatial regime at once in an easily perceptible way. In particular, in addition to the shape and orientation of the tensor, the trace and isotropy of the diffusion tensor field is depicted as well by intrinsic means, which is of crucial importance for analysis of tissues harboring a tumor. The method moreover provides good robustness against possible artifacts due to numerical integration schemes, data interpolation methods, eigenvector ambiguities, and instrumental noise.

The techniques have been successfully used for analysis of diffusion tensor fields from magnetic resonance image acquisition. The visual appearance of a tumor within a human brain, its medical relevance and causation on a cellular basis were discussed.

REFERENCES

- Aldroubi, A., & Basser, P. J. (1999). Reconstruction of vector and tensor fields from sampled discrete data. In: D. Larson & L. Baggett (Eds.), *The functional and harmonic analysis of wavelets, contemporary mathematics, vol. 247* (pp. 1–15). Providence, RI: American Mathematical Society.
- Bailey, P., & Cushing, H. W. (1926). *A classification of the tumors of the glioma group on a histogenetic basis with a correlated study of prognosis*. Philadelphia, PA: J. B. Lippincott.
- Basser, P. J., Pajevic, S., Pierpaoli, C., Duda, J., & Aldroubi, A. (2000). In vivo fiber tractography using dt-mri data. *Journal of Magnetic Resonance*, *44*, 625–632.
- Bell, A. J., & Sejnowski, T. J. (1996). Edges are the “independent components” of natural scenes. *Advances in Neural Information Processing Systems*, *9*, Cambridge, MA: MIT Press.
- Benger, W., & Hege H.-C. (2003). Analyzing curved spacetimes with tensor splats. Paper presented at the *10th Marcel Grossmann Meeting*, Rio de Janeiro, July 20–26, 2003, <http://www.zib.de/visual/publications/sources/MGX.pdf>.
- Benger, W., & Hege H.-C. (2004). Tensor splats. In R. F. Erbacher, P. C. Chen, J. C. Roberts, M. Grohn, & K. Borner (Eds.), *Conference on Visualization and Data Analysis 2004, Proceedings of SPIE*, 5295 IS&T/SPIE Electronic Imaging Symposium in San Jose, CA. pp. 151–162.

- Berry, C. L. (Ed.) (1988). *Neuropathology*. New York, NY: Springer-Verlag.
- Bhalerao, A., & Westin C.-F. (2003). Tensor splats: Visualizing tensor fields by texture mapped volume rendering. In *Sixth international conference on medical image computing and computer-assisted intervention (MICCAI'03)*, Montreal, Canada, November 2003, pp. 294–901.
- Bingham, C. (1974). An antipodally symmetric distribution on the sphere. *Annals of Statistics*, 2, 1201–1225.
- Bruhlmeier, M., Roelcke, U., Brauenstein, P., Missimer, J., Schubiger, P. A. Locher, J. Th., Pellikka, R., & Ametamey, S. M. (2003). Measurement of the extracellular space in brain tumors using 76br-bromide and PET. *Journal of Nuclear Medicine*, 44, 1210–1218.
- Ciric, I., Ammirati, M., Vick, N., & Mikhael, M. (1987). Supratentorial gliomas: Surgical considerations and immediate postoperative results. Gross total resection versus partial resection. *Neurosurgery*, 21, 21–26.
- Crawfis, R. A., & Max, N. L. (1993). Texture splats for 3d scalar and vector field visualization. *IEEE Visualization 1993*, 261–267.
- Einstein, A. (1905). Über die von der molekularkinetischen Theorie der wärme geforderte Bewegung von in ruhenden Flüssigkeiten suspendierten Teilchen. *Annals of Physics*, 17, 549–560.
- Einstein, A. (1916). Die Grundlage der allgemeinen Relativitätstheorie. *Annalen der Physik* 4, 284–339.
- Field, A. S., Alexander, A. L., Wu, Y.-C., Hasan, K. M., Witwer, B., & Badie B. (2004). Diffusion tensor eigenvector directional color imaging patterns in the evaluation of cerebral white matter tracts altered by tumor. *Journal of Magnetic Resonance Imaging*, 20, 2004.
- Gabor, D. (1946). Theory of communication. *Journal of the Institute for Electrical Engineers*, 72, 429–459.
- Haber R. B. (1990). Visualization techniques for engineering mechanics. *Computer Systems in Engineering*, 1, 37–50.
- Hornak, J. P. (2004). *Basics of MRI*. Rochester, NY: Rochester Institute of Technology, <http://www.cis.rit.edu/htbooks/mri/>
- Hubel, D. H., & Wiesel, T. N. (1962). Receptive fields, binocular interaction and functional architecture in the cat's visual cortex. *Journal of Physiology (London)*, 160, 106–154.
- Jähne, B. (1997). *Practical handbook on image processing for scientific applications*. Boca Raton, FL: CRC Press.
- Jones, J. P., & Palmer, L. A. (1987). The two-dimensional spatial structure of simple receptive fields in cat striate cortex. *Journal of Neurophysiology*, 58, 1187–1211.
- Jupp, P. E. (2001). Modifications of the Rayleigh and Bingham tests for uniformity of directions. *Journal of Multivariate Analysis*, 77, 1–20.
- Kindlmann, G., & Weinstein, D. (1999). Hue-balls and lit-tensors for direct volume rendering of diffusion tensor fields. *Visualization '99*, 183–189.

- Kindlmann, G., & Weinstein, D., & Hart, D. (2000). Strategies for direct volume rendering of diffusion tensor fields. *IEEE Transactions on Visualization and Computer Graphics*, *6*, 124–138.
- Kindlmann, G. (2004). Superquadric tensor glyphs. *Joint Eurographics—IEEE TVCG Symposium on Visualization* (“VisSym”), 2004.
- Kiwit, J. C., Floeth, F. W., & Bock, W. J. (1996). Survival in malignant glioma: Analysis of prognostic factors with special regard to cytoreductive surgery. *Zentralblatt für Neurochirurgie*, *57*, 76–88.
- Kleihues, P., Burger, P. C., & Scheithauer, B. W. (1993). The new WHO classification of brain tumors. *Brain Pathology*, *3*, 255–268.
- Laidlaw, D. H., Ahrens, E. T., Kremers, D., Avalos, M. J., Jacobs, R. E., & Readhead, C. (1998). Visualizing diffusion tensor images of the mouse spinal cord (pp. 127–134), June 1998.
- Le Bihan, D., Breton, E., Lallemand, D., Grenier, P., Cabanis, E., & Laval-Jeantet, M. (1986). MR imaging of intravoxel incoherent motions: Application to diffusion and perfusion in neurologic disorders. *Radiology*, *161*, 401–407.
- Le Bihan, D., Breton, E., Lallemand, D., Aubin, M. L., Vignaud, J., & Laval-Jeantet, M. (1988). Separation of diffusion and perfusion in intravoxel incoherent motion MR imaging. *Radiology*, *168*, 497–505.
- Lehmann, T., Gönner, C., & Spitzer, K. (1999). Survey: Interpolation methods in medical image processing. *IEEE Transactions on Medical Imaging*, *18*, 1049–1075.
- Lehmann, T., Gönner, C., & Spitzer, K. (2001). Addendum: Spline interpolation in medical image processing. *IEEE Transactions on Medical Imaging*, *20*, 660–665.
- Lysaker, M., Lundervold, A., & Tai, X. (2003). Noise removal using fourth-order partial differential equations with applications to medical magnetic resonance images in space and time. *IEEE Transaction on Image Processing*, *12*, 1579–1590.
- Mardia, K. V., & Jupp, P. E. (2000). *Directional statistics. Wiley series in probability and statistics*. New York: Wiley.
- Meijering, E. (2002). A chronology of interpolation: From ancient astronomy to modern signal and image processing. *Proceedings of the IEEE*, *90*, 319–342.
- Moakher, M., & Batchelor, P. G. (2006). Symmetric positive definite matrices: From geometry to applications and visualization. In J. Weickert & H. Hagen (Eds.), *Visualization and Image Processing of Tensor Fields*. Berlin, Heidelberg, New York: Springer.
- Mojsilovic, A., Kovacevic, J., Safranek, R. J., Hu, J., & Ganapathy, K. (2000). Matching and retrieval based on the vocabulary and grammar of color patterns. *IEEE Trans. on Image Processing*, *9*, 38–54.
- O’Donnell, L., Haker, S., & Westin, C.-F. (2002). New approaches to estimation of white matter connectivity in diffusion tensor MRI: Elliptic PDEs and geodesics in a tensor-warped space. In *Fifth international conference on medical image computing and computer-assisted intervention (MICCAI’02)* Tokyo, Japan, 2002, pp. 459–466.

- Osher, S., Sole A., & Vese, L. (2003). Image decomposition and restoration using total variation minimization and the H-1 norm. *SIAM Journal on Multiscale Modeling and Simulation*, 1, 349–370.
- Özarslan, E., & Mareci, T. H. (2003). Generalized diffusion tensor imaging and analytical relationships between diffusion tensor imaging and high angular resolution diffusion imaging. *Magnetic Resonance in Medicine*, 50, 955–965.
- Pajevic, S. Aldroubi, A., & Basser, P. (2002). A continuous tensor field approximation of discrete DT-MRI data for extracting microstructural and architectural features of tissue. *Journal of Magnetic Resonance*, 154, 85–100.
- Pajevic, S., Aldroubi, A., & Basser, P. J. (2005). Continuous tensor field approximation of diffusion tensor MRI data. In J. Weickert & H. Hagen, (Eds.), *Visualization and image processing of tensor fields*. Berlin, Germany: Springer.
- Poirson, A., & Wandell, B. (1996). Pattern-color separable pathways predict sensitivity to simple colored pattern. *Vision Research*, 36, 515–526.
- Price, S. J., Pena, A., Burnet, N. G., Jena, R., Green, H. A., Carpenter, T. A., Pickard, J. D., & Gillard, J. H. (2004). Tissue signature characterisation of diffusion tensor abnormalities in cerebral gliomas. *European Radiology*, 14, 1909–1917.
- Ries, L. A. G., Eisner, M. P., Kosary, C. L., Hankey, B. F., Miller, B. A., Clegg, L., & Edwards, B. K. (Eds.) (2002). *Seer Cancer Statistics Review, 1973–1999*. Bethesda, MD: National Cancer Institute.
- Rudin, L., Osher, S., & Fatemi, E. (1992). Nonlinear total variation based noise removal algorithms. *Physica D*, 60, 259–268.
- Scerrati, M., Roselli, R., Iacoangeli, M., Pompucci, A., & Rossi, G. F. (1996). Prognostic factors in low grade (WHO grade II) gliomas of the cerebral hemispheres: The role of surgery. *Journal of Neurology, Neurosurgery, and Psychiatry*, 61, 291–296.
- Schutz, B. F. (2003). *Gravity from the ground up*. New York: Cambridge University Press.
- Stejskal, E. O., & Tanner, J. E. (1965). Spin diffusion measurements: Spin echoes in the presence of a time dependent field gradient. *The Journal of Chemical Physics*, 42, 288–292.
- Tuch, D. S., Weisskoff, R. M., Belliveau, J. W., & Wedeen, V. J. (1999). High angular resolution diffusion imaging of the human brain. *Proceedings of the 7th Annual Meeting of ISMRM*, 24 May to 28 May 1999, Philadelphia, PA, p. 321.
- Unser, M., Aldroubi, A., & Eden, M. (1992). Polynomial spline signal approximations: Filter design and asymptotic equivalence with Shannons sampling theorem. *IEEE Transactions on Information Theory*, 38, 95–103.
- Unser, M., Aldroubi, A., & Eden, M. (1993a). B-spline signal processing: Part I theory. *IEEE Transactions on Signal Processing*, 41, 821–833.
- Unser, M., Aldroubi, A., & Eden, M. (1993b). B-spline signal processing: Part II efficient design and applications. *IEEE Transactions on Signal Processing*, 41, 834–848.

- Vargova, L., Homola, A., Zamecnik, J., Tichy, M., Benes, V., & Sykova, E. (2003). Diffusion parameters of the extracellular space in human gliomas. *Glia*, *42*, 77–88.
- Wandell, B. (1993). Color appearance: The effects of illumination and spatial pattern. *Proceedings of the National Academy of Science of the USA*, *10*, 2458–2470.
- Watson, A. B., & Turano, K. (1995). The optimal motion stimulus. *Vision Research*, *35*, 325–336.
- Watson, A. B., & Turano, K. (1995). The optimal motion stimulus. *Vision Research*, *35*, 325–336.
- Weickert, J. (2006). Tensor field interpolation with PDEs. In J. Weickert & H. Hagen (Eds.), *Visualization and image processing of tensor fields*. New York: Springer.
- Weinstein, D., Kindlmann, G., & Lundberg, E. (1999). Tensorlines: advection-diffusion based propagation through diffusion tensor fields. In *Proceedings of Visualization '99* (pp. 249–253). Los Alamitos, CA: IEEE Computer Society Press.
- Westin, C. F., Peled, S., Gudbjartsson, H., Kikinis, R., & Jolesz, F. A. (1997). Geometrical diffusion measures for MRI from tensor basis analysis. In *Proceedings of ISMRM, Fifth Meeting* (p. 1742). Vancouver, Canada.
- Westin, C. F., Maier, S. E., Mamata, H., Nabavi, A., Jolesz, F. A., & Kikinis, R. (2002). Processing and visualization for diffusion tensor MRI. *Medical Image Analysis*, *6*, 93–108.
- Westover, L. (1990). Footprint evaluation for volume rendering. *SIGGRAPH'90: Proceedings of the 17th annual conference on computer graphics and interactive techniques Dallas, TX, USA* (pp. 367–376). New York: ACM Press.
- Wiegell, M. R., Larsson, H. B., & Wedeen, V. J. (2000). Fiber crossing in human brain depicted with diffusion tensor MR imaging. *Radiology*, *217*, 897–903.
- Witwer, B. P., Moftakhar, R., Hasan, K. M., Deshmukh, P., Haughton, V., Field, A., Arfanakis, K., Noyes, J., Moritz, C. H., Meyerand, M. E., Rowley, H. A., Alexander, A. L., & Badie, B. (2002). Diffusion-tensor imaging of white matter tracts in patients with cerebral neoplasm. *Journal of Neurosurgery*, *97*, 568–575.
- Wu, Y.C., Field, A. S., Chung, M. K., Badie, B., & Alexander, A. L. (2004). Quantitative analysis of diffusion tensor orientation: Theoretical framework. *Magnetic Resonance in Medicine*, *52*, 1146–1155.
- Year 2001 Annual Statistics Report. (2001). *Brain tumors in the United States 1992–1997*. World Wide Web: http://www.cbtrus.org/2001/2001stats_report.htm
- Zheng, X., & Pang, A. (2004). Topological lines in 3d tensor fields. In: *Proceedings of Visualization 2004*. Los Alamitos, CA: IEEE Computer Society Press.